Abstract

The optical spectrometer is an instrument used to measure the spectrum of an input light source, characterizing its wavelengths and intensities. Spectrometers have important applications in a variety of fields including chemical and biological composition analysis, space exploration. However, conventional spectrometers use long focal lengths to achieve high precision, which makes them large and expensive. The size and cost limit their applications. Therefore, the miniaturization of spectrometers is an important topic, and there have been many contributions made to on-chip size spectrometers in the last decades. One obstacle is that most of these small-size spectrometers are suffering from fabrication errors, preventing them from reaching the designed precision. In the previous work from Tanabe's group, we presented a reconstructive spectrometer using random photonic crystal waveguides. The structural randomness of the photonic crystal from fabrication error causes wavelength-sensitive light localization patterns, which can be used to reconstruct the input spectrum by an algorithm.

In this work, we continue to develop the device by investigating its geometry parameters like waveguide section length, section width reduction rate, and disorder level. We make numerical simulations for designs with different parameters and analyze their performances as spectrometers. The target is to find some ranges of parameters to achieve an optimal balance between resolution, spectral range, and physical size for our on-chip spectrometer. The development of on-chip spectrometers has potential applications in new fields such as portable sensing devices, and we hope this work can pave the way for a low-cost and mass-produced on-chip spectrometer.

Chapter 1 presents the background of the research.

Chapter 2 describes the basic theory of photonic crystal waveguide and Anderson localization, how they are utilized to design a reconstructive spectrometer, as well as the objective of this work.

Chapter 3 introduces the simulation method and setups used for this work.

Chapter 4 numerically investigates how the geometry parameters affect the performance of the spectrometer by showing simulation results.

Chapter 5 summarizes the work and discusses future issues of the research.

Contents

List of Figures

List of Abbreviations

FWHM	Full Width at Half Maximum
MEMS	Micro Electro Mechanical Systems
SNR	Signal-to-Noise Ratio
MZI	Mach-Zehnder Interferometer
SOI	Silicon-On-Insulator
SWIFTS	Stationary Wave Integrated Fourier Transform Spectrometer
SEM	Scanning Electron Microscope
FSR	Free Spectral Range
CWL	Center Wavelength
FDTD	Finite-Difference Time-Domain
PhC	Photonic Crystal
QD	Quantum Dot

Chapter 1

Introduction

1.1 Background of optical spectrometer

An optical spectrometer is a scientific characterization instrument that can measure physical properties of an input light over a specific electromagnetic spectrum range. It usually measures the wavelengths and intensities of light, producing spectral lines. Because of the fact that each element in the periodic table has a unique emission or absorption light spectrum, optical spectrometers have served as one of the most important exploratory tools for composition analysis in many fields like physics, chemistry and astronomy.

The famous early study of spectroscopy is Issac Newton's experiment of splitting up white light into component colors by refraction through a prism. The rainbow colors can be re-combined into a white light through another prism, which proves that the colors are separated from white light rather than newly generated by the prism. The word "spectrum" was first applied by Newton and he is generally regarded as the founder of spectroscopy.

Modern benchtop laboratory spectrometers are generally dispersive-type that contains bulky and expensive optical components, moving parts, and long optical paths. Due to the intrinsic feature of dispersive optics, longer focal lengths lead to more separated wavelengths when reaching detector arrays and reliably increase the resolution of spectrometers, which is the first priority in laboratory situations. However there are also demands of spectrometers in outdoor or industrial situations where indicative, instantaneous results are preferable than transporting samples to a laboratory and waiting for ultra-high resolution results. For example, the soil analysis, monitoring of food industry production lines. In these cases, the size, cost and power consumption of conventional laboratory spectrometers limit their applications. Therefore, the miniaturization of spectrometers is a crucial topic that can open up the possibilities of spectrometer for up-coming applications like smartphone-based and wearable devices.

1.2 Miniaturization of spectrometer

Since the early 1990s, miniaturized optical spectrometers have been developed for decades, and can be roughly summarized into four categories.

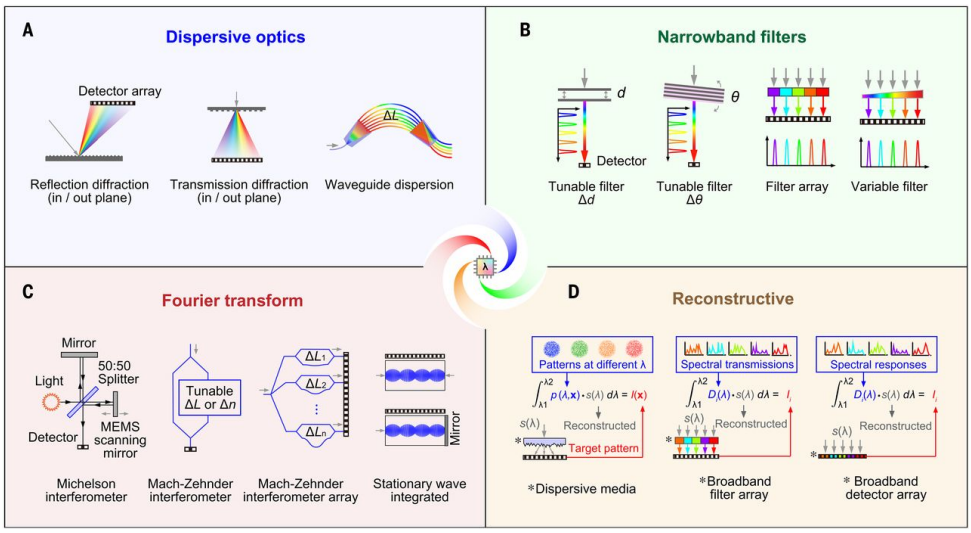

Figure 1.1: Different underlying strategies for miniaturized spectrometer systems that have emerged over the past 30 years. From Ref. [1]. (A) Miniaturized dispersive optics type. (B) Tunable or arrayed narrowband filters type. (C) Fourier transform type. (D) Computational spectral reconstruction type.

1.2.1 Dispersive optics type

Dispersive optics that split light towards spatially separated detectors are the earliest methods used for spectrometers. The dispersions were compromised by prisms in early days. In modern conventional spectrometers, the task is usually accomplished by a diffraction grating, combined with an optical path and a detector array.

Light incident on a grating is diffracted following the equation:

$$d(\sin\alpha \pm \sin\beta) = m\lambda \tag{1.1}$$

where λ is the light's wavelength, d is the spacing between grooves on the grating, α is the incident angle of light, and β is the diffracted angle of the light leaving the grating. The left side of Equation 1.1 represents the path difference between wavefronts diffracted from two neighboring grooves, where the $\pm$ sign will be plus for reflection grating and minus for transmission grating. When m is an integer, constructive interference happens for diffracted light wavefronts, and light with diffracted angle β can be observed and collected.

Advancements in micro and nano fabrication technologies make it possible to scale down dispersive spectrometers to on-chip sizes with reasonable costs. The challenges are concentrated on the miniaturization of three key components: the diffraction grating, the optical path, and the detector array. The decrease of optical path length significantly helps miniaturize the footprint of the device, but can severely lower the spectral resolution at the same time. Researchers have came up with various methods to compensate the problem. For example, use concave gratings to save the space of collimation components and focus light to detector elements to

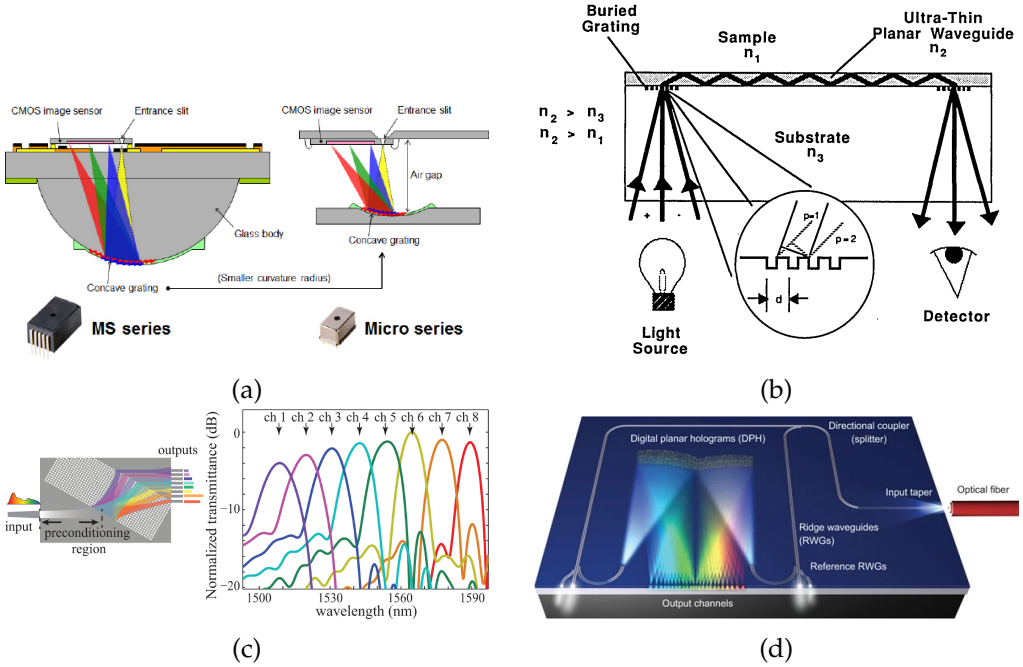

Figure 1.2: Dispersive optics type microspectrometers. (a) Schematic of a reflective concave grating. From Ref. [2]. (b) Schematic of a buried grating under a planar waveguide. From Ref. [3]. (c) Schematic of a photonic crystal-based grating. From Ref. [4]. (d) Schematic of a planar holograms-based grating. From Ref. [5].

increase the resolution [2], use internal reflections of planar waveguide to compress the free space dimension of optical paths [3]. There are also waveguide-based in-plane solutions that use planar photonic crystals [4] or planar holograms [5] as dispersion components.

Besides improving the configurations of diffraction grating and optical path, increasing the detector's density within a given area is another direction to enhance the spectral resolution of spectrometer. However, as the scale decreases, the quality of both diffraction grating and detector array becomes much more sensitive to fabrication errors like etching-induced surface roughness, preventing the expected behavior of disperive optics and limiting further increase of spectral resolution.

1.2.2 Narrowband filter type

A narrowband filter can selectively transmit light within a specific wavelength range, producing a narrowband spectral line. Using a tunable narrowband filter with time varying transmissive properties, or an array of multiple narrowband filters with unique transmitted wavelengths each, the spectrometer can operate over a consecutive wavelength range. A key advantage of narrowband filters type spectrometers over dispersive optics type systems is that the optical path length doesn't affect the spectral resolution dominantly. The separation between filters and detectors can

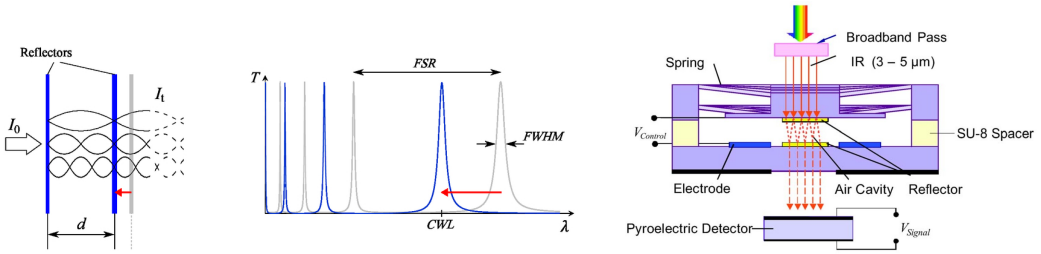

(a) (b)

Figure 1.3: Tunable narrowband filter-based spectrometers. (a) Left: Schematic and working principle of the Fabry-Pérot interferometer. Right: Transmission spectra of the Fabry-Pérot interferometer (CWL: center wavelength, FSR: free spectral range, FWHM: full width at half maximum). From Ref. [6]. (b) Schematic of a tunable Fabry-Pérot filter with MEMS electrostatic actuators. From Ref. [7].

be made extremely small, thus dramatically reduce the footprint of whole system.

A typical structure for tunable narrowband filter is the Fabry-Pérot optical cavity made from two parallel mirrors. The spectral response of a Fabry-Pérot resonator is based on interference between the light injected in and the light reflected by mirrors. Only when the optical distance between the two mirrors is an integral multiple of the light's half wavelength $\lambda/2$, constructive interference occurs and the light is resonated and has maximum transmittance. The response of a Fabry-Pérot filter can be described by spectral lines with Airy distributions. The spectral resolution of these Fabry-Pérot spectrometers is decided by the FWHM (full width at half maximum) of transmission peaks, and the transmission spectra can be tuned during operation by varying the optical path length. The most common way is using MEMS (micro electro mechanical systems) structures to tuning the separation distance between two mirrors by an electrostatic [7][10] or piezoelectric [11] actuator.

The tunable narrowband filter spectrometer can operate with a single filter, but the spectra has to be scanned in a time sequence. In applications where instantaneous measurements are required, narrowband filter arrays and linear variable filters can offer high-speed multiplex measurements, at the cost of adding space for filters and detector arrays.

For filter array type, the filter array and detector array are generally bijective, each filter element is responsible for selecting and transmitting a specific wavelength to its paired detector. The number of detection channels directly constrains the resolution or spectral range of the spectrometer. Various technologies for filter arrays have been developed, such as Fabry-Pérot etalons [8], thin films [12], planar photonic crystals [13], photonic bandgap fibers [9], metasurfaces [14], and waveguide ring resonators [15] [1].

The linear variable filter is a variant of filter array. Instead of filtering the wavelengths discretely, a linear variable filter can produce consecutive spectra along one axis of the filter, which can be realized by a tapered cavity

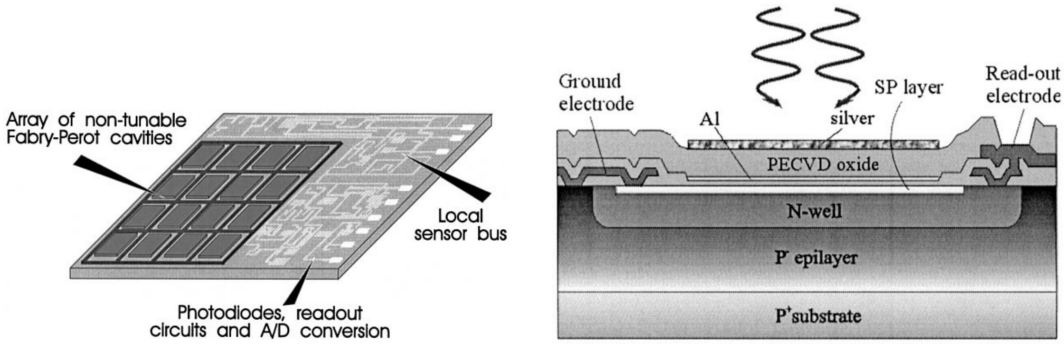

(a) (b)

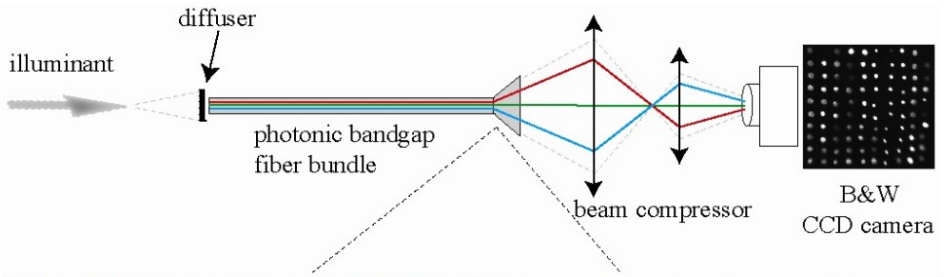

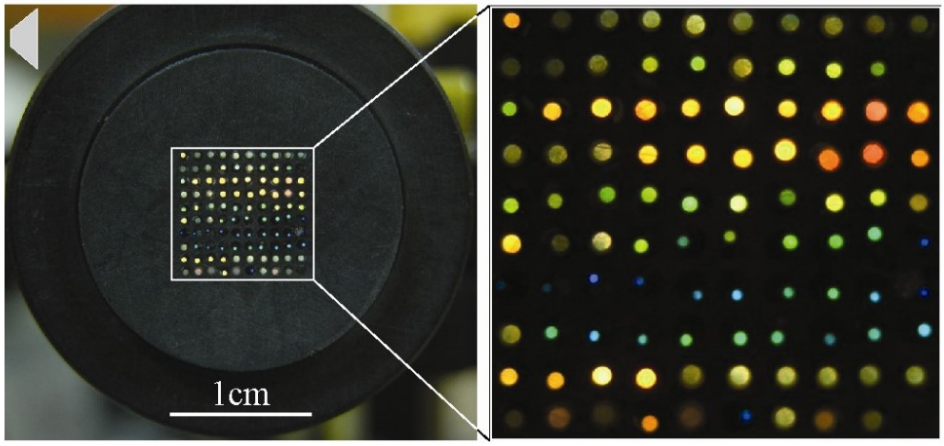

(c)

Figure 1.4: Filter array-based spectrometers. (a) A single-chip integrated with an array of non-tunable Fabry-Pérot etalons, photodiodes, read-out circuits and the bus interface. (b) Cross-section of a CMOS Fabry-Pérot etalon with the photodiode underneath. From Ref. [8]. (c) Schematic of a photonic bandgap fiber bundle spectrometer. From Ref. [9].

[16] or tapered waveguide [17].

1.2.3 Fourier transform type

Fourier transform type spectrometers use interferometers to modulate the incident light, collect time-variant light intensities, and calculate spectra via Fourier transform. The early Fourier transform type spectrometers are based around Michelson interferometers. The incident light is divided by a beam splitter into two arms, one towards a fixed mirror and the other towards a movable mirror. Both light beams are reflected back toward the beam splitter and the recombined beam is directed to the detector. Because of the phase difference induced by optical path length difference Δ between the two arms, a interference pattern is generated and its time-variant intensities are measured by the detector. By making measurements of the signal at many discrete positions of the moving mirror, an interferogram as a function of optical path length difference Δ is generated, an a Fourier transform can convert the interferogram into a spectrum of incident light. Since Fourier transform spectrometers avoid spatial dispersion of light and monitor all wavelengths simultaneously on the detector, the signal-to-noise ratio (SNR) receives an increase, offering an inherent advantage over dispersion optics spectrometer.

The Michelson interferometer can be miniaturized by applying MEMS to manipulate the movable mirror [18]. A drawback of the Michelson interferometer for miniaturization is that the spectral resolution is limited by the maximum path length difference allowed by the actuator travel range. In recent years, the mainstream of planar on-chip Fourier transform spectrometer is based on waveguides and interferometers without movable mirrors. The typical structure is Mach-Zehnder interferometer (MZI), in which light is split into two waveguide pathways and recombined before reaching a single detector. The optical path length difference between the pathways can be modulated via several methods, for example, the electro-optic modulation of $LiNbQ_3$ waveguides [22][19], or integrating microheaters adjacent to optical pathways to exploit thermo-optical effects, which has been demonstrated on silicon-on-insulator (SOI) waveguides [20][23].

Another approach of miniaturized interferometer-based spectrometer is the stationary wave integrated Fourier transform spectrometer (SWIFTS), which uses a dual temporal and spatial sampling scheme. In SWIFTS, a standing wave is set up through two counter-propagating light in a waveguide. By depositing metallic nano-probes on top of the waveguide to sample the evanescent fields, temporal and spatial interferograms can be measured at the same time. Furthermore, by applying a voltage to induce electro-optic effects, the spatial interferogram can be shifted along the waveguide, solving the undersampling problem of limited detector numbers [21].

In general, on-chip Fourier transform type spectrometers require some active control on the interferometers to sample temporal or spatial

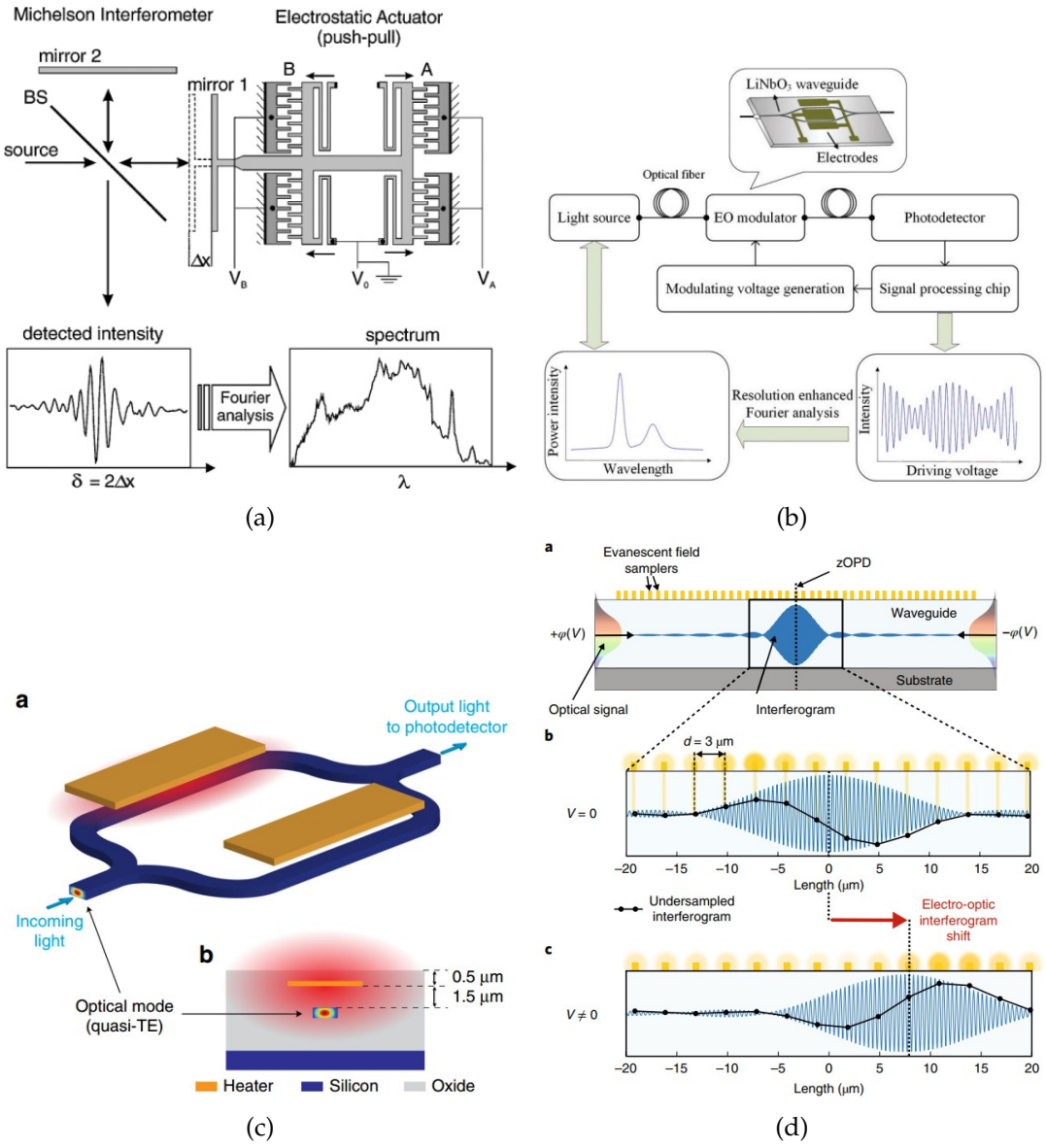

Figure 1.5: Fourier transform type microspectrometers. (a) Schematic of a miniaturized Michelson interferometer-based Fourier transform spectrometer with a MEMS electrostatic actuator. From Ref. [18]. (b) Schematic of a MZI-based Fourier transform spectrometer using a $LiNbO_3$ waveguide with electro-optic modulation. From Ref. [19]. (c) Schematic of a MZI-based Fourier transform spectrometer using thermal-optical effects to modulate optical path difference. From Ref. [20]. (d) Schematic of a stationary wave integrated Fourier transform spectrometry (SWIFTS) system using the electro-optic effect in $LiNbO_3$ to shift the interferogram along the waveguide over time through a bias voltage. From Ref. [21].

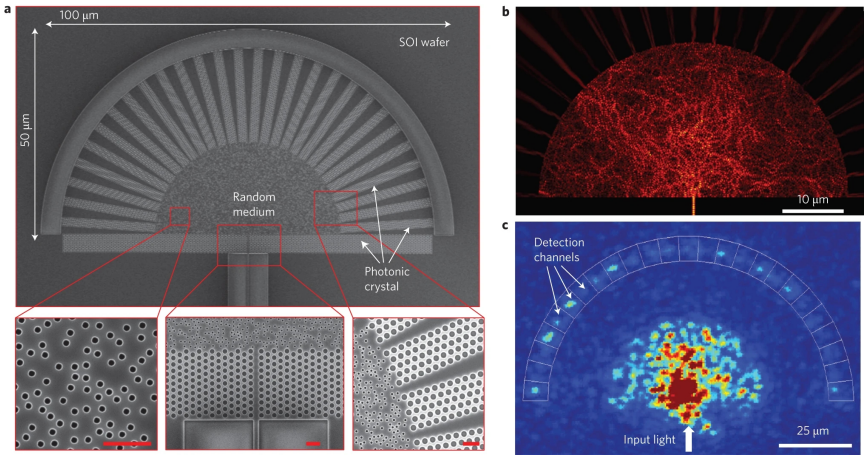

Figure 1.6: An on-chip-size spectrometer based on multiple scattering in a random disordered photonic crystal region. From Ref. [24]. (a) SEM image of the fabricated spectrometer. The dispersive element is a semicircular region of randomly positioned air holes. The probe signal is coupled into the random medium via a defect waveguide at the bottom of the semicircle, then diffuses through the random medium via multiple scattering and eventually reaches the 25 defect waveguides around the circumference of the semicircle. These tapered waveguides will couple the signals to the detection channels. (b) Numerical simulation of light path of TE polarized light at $\lambda = 1{,}500$ nm. (c) Experimental near-infrared optical image of the random spectrometer with a probe signal at $\lambda = 1{,}500$ nm.

interferograms. It has some advantages like high SNR. The spectral range and resolution of such spectrometer are determined by sampling size and rate, which usually rely on the performance of actuators in interferometers. Aside the challenges from the miniaturization of interferometers, the computation effort of Fourier transform may affect its time response when comparing with other types of spectrometers.

1.2.4 Reconstructive type

In a conventional grating-based or filter-base spectrometer, each wavelength in the spectrum is mapped to an individual detector, so the spectral resolution is directly decided by the number of detection channels. As the footprint of device scales down, this one-to-one mapping constrains the spectral resolution due to fabrication techniques, including the density of detectors in a limited space and the fabrication errors of detector array.

To overcome the limitations of such one-to-one mapping, an alternative approach is to realize complex spectral-to-spatial mapping by random disordered structures. The working principle of random spectrometers is that the characteristic pattern formed by transmitted light through a disordered system provides a sort of fingerprint, uniquely identifying the wavelength of transmitted light. The characteristic patterns are usually one- or two dimensional spatial intensity distributions and can be used to reconstruct the input spectrum. For example, in the work presented by

Redding et al.[24], as shown in Figure 1.6, a semicircle region of random photonic crystal scatter is designed to let each input wavelength goes through unique propagation paths and reach specific detection channels, where the combination of intensities measured by detection channels can be used as characteristic patterns to reconstruct the input spectrum. In their another work, an evanescently coupled multimode spiral waveguide can form wavelength-dependent speckle pattern from the interference between the modes in the waveguide, and evanescent coupling between neighboring arms of the spiral results in a non-resonant broadband enhancement of the spectral resolution [25].

The reconstruction of input spectrum is essentially the solution of a linear equation problem, which can be expressed as

$$\boldsymbol{I} = \boldsymbol{T} \cdot \boldsymbol{S} \tag{1.2}$$

where $\boldsymbol{I}$ is the measured intensity vector, $\boldsymbol{S}$ is the input spectrum vector, and $\boldsymbol{T}$ is the transfer matrix which contains the complex spectral-to-spatial mapping information. In practical, the measured intensity is the linear overlay of scaled characteristic patterns of all wavelengths, and the target spectrum can be understand as the assembly of scaling weights of their intensity patterns.

After the fabrication of a reconstructive spectrometer, there is always a calibration step necessary to correctly obtain the transfer matrix $\boldsymbol{T}$. This can be achieved by using monochromatic probe lights to scan over the spectral range to get the characteristic intensity pattern for each wavelength, which refers to a specific column in the transfer matrix $\boldsymbol{T}$. The reconstructive spectrometers are highly robust with respect to fabrication errors, which are compensated for through calibration. However, the operating temperature usually requires precise control to ensure the transfer matrix works.

If the characteristic patterns of two distinct wavelengths are identical, it is impossible to tell the input spectrum $\boldsymbol{S}$ from the measured intensity $\boldsymbol{I}$. On the contrary, the higher the dissimilarity between the characteristic patterns, the higher resolving power the spectrometer has, which mathematically refers a transfer matrix $\boldsymbol{T}$ with diverse columns. In practical, the inversion problem is typically ill-posed, which can be overdetermined or underdetermined if the number of detectors is higher or lower than the number of data points in the reconstructed spectrum, respectively. In the overdetermined case, truncation of the measured data that is easily affected by the noise can effectively suppress reconstruction errors. In the underdetermined case, additional information such as smoothness can be adopted to approximate the best possible solutions. Techniques like compressive sensing [26] and machine-learning [27] are also promising methods to improve the spectral resolutions.

1.3 Objective of this study

As described in the earlier section, reconstructive type spectrometer has great attractions over other categories of miniaturized spectrometer, such

as the enhancement of resolution on limited device footprint by complex spectral-to-spatial mapping, high robustness to fabrication imperfections through calibration, and the potential of further improved performance by optimizing reconstruction algorithms. The cost-performance ratio of reconstructive type spectrometer will definitely benefit from the increases in computational power, reductions in processor price and size, and the development of computational software. Therefore, reconstructive type spectrometer is a promising direction to achieve high resolution, wide spectral range, and ultra-compact physical footprint.

In this study, we are interested in using the simple photonic crystal slab waveguide as the structure of a reconstructive type spectrometer, by using the inherent fabrication imperfections induced Anderson localization as the characteristic pattern for reconstruction. The feasibility of this idea has been demonstrated and the performance of a prototype has been measured experimentally by Kodama et al. from Tanabe Lab [28]. The details of the random photonic crystal waveguides-based reconstructive spectrometer will be explained in Chapter 2. The objective of this thesis is a quantitative numerical investigation of geometry parameters for this spectrometer, by controlling variables and comparing its performances at varying parameters. The numerical simulation method and setups will be described in Chapter 3. Then the simulation results and analyses will be shown in Chapter 4. Finally, in Chapter 5, the study will be summarized and the outlook of this spectrometer design will be discussed.

Chapter 2

Theory of Random Photonic Crystal Waveguide-Base Reconstructive Spectrometer

2.1 Photonic crystal waveguide

The photonic crystal is an optical nanostructure which has periodicity in its refractive index. Depending on the periodicity, the photonic crystal can be 1-dimensional, 2-dimensional, or 3-dimensional. Simple examples that show the concept of photonic crystal waveguide is shown in Figure 2.1. In this work, we focus on 2-dimensional photonic crystal structures which are easy to fabricate.

Photonic crystals receive great interest because of their potential to manipulate the propagation of light. The optical band structure of a photonic crystal can be artificially designed by adjusting its materials and periodicity.

An important feature of photonic crystals' band structure is the band gap, as shown in Figure 2.2 in which the propagation of light is forbidden in one or multiple directions.

A photonic crystal (PhC) waveguide is created by introducing a line defect to the 2-dimensional photonic crystal by removing a row of airholes, the periodicity of the photonic crystal is partially broken, which creates propagating modes inside the photonic crystal band gap. These modes can only propagate along the line defect because of the constraint of the photonic

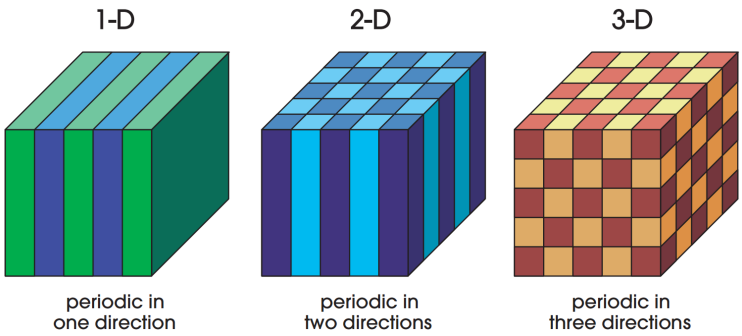

Figure 2.1: Simple examples that show periodic structures of one-, two-, and three dimensional photonic crystals. The different colors represents materials with different dielectric constants. From Ref. [29].

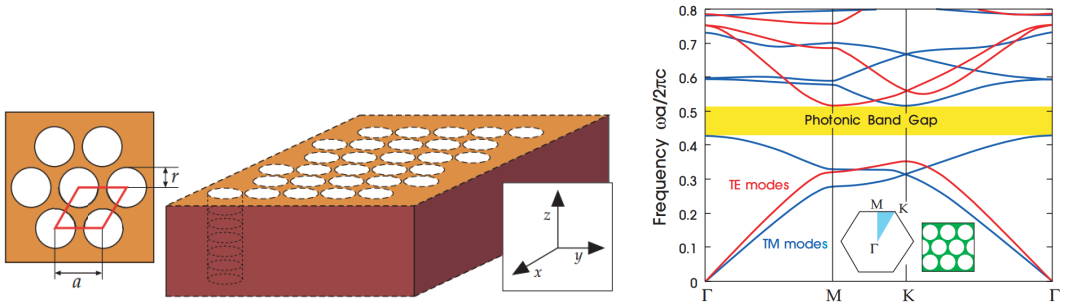

(a) (b)

Figure 2.2: (a) A two-dimensional photonic crystal with triangular lattice air columns in a dielectric substrate. (b) An example of band structure of a two-dimensional triangular lattice photonic crystal, which consists of a TE photonic band gap. From Ref. [29].

crystal band gap in other in-plane directions and total internal reflection in out-of-plane directions, which makes the photonic crystal slab with a line defect behave like a waveguide.

Compared with general slab waveguides which utilize total internal reflection at the boundaries of core and coating medium, photonic crystal waveguides have better compatibility with sharp bends because the constraint of photonic crystal band gap can suppress losses at bends. In addition, the band structure of photonic crystal waveguide can be modified by changing parameters like lattice constant, lattice shape, refractive index, and line defect width, providing great flexibility for designing waveguides with expected behaviours. Besides, the dispersive curve of the guided mode allows slow-light regime at near-cut-off wavelengths [30], which has applications such as enhancing light-matter interaction.

2.2 Fabrication errors and Anderson localization in PhC waveguide

In previous section, we mentioned that photonic crystal is a nanostructure whose refractive index periodically changes in one or multiple directions. This periodicity generates many interesting features of photonic crystal structures. However, in practical situations, there is no perfect photonic crystal, no matter it is natural or artificial structure, there are always more or less statistical errors in the form of variations relative to the ideal structure. Although it is known that photonic crystal is robust to small imperfections, it may become a sensitive problem for the precise nanostructure applications like slow-light transport or single-photon sources. Therefore, the effects of these unavoidable random disorders deserve some thorough investigations, and people even found some approaches to induce new functionalities by random disorders. In this section, we focus on disorder induced Anderson localization in photonic crystal (PhC) waveguides.

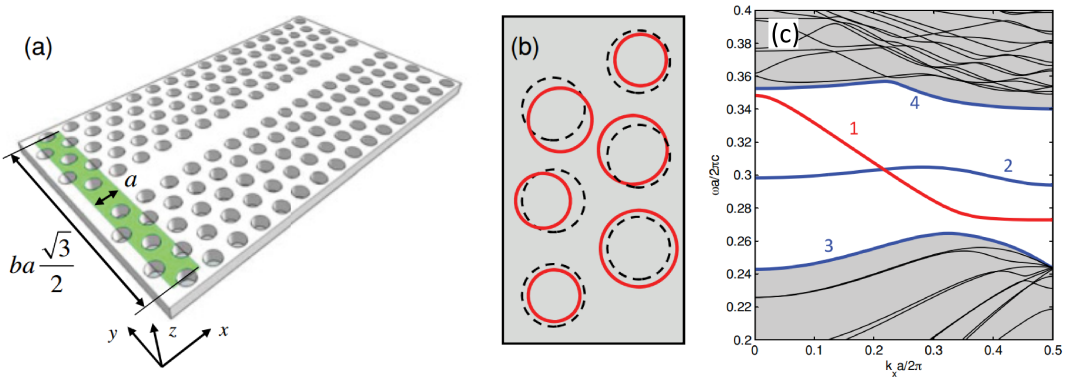

Figure 2.3: (a) Sketch of the W1 line-defect photonic crystal waveguide. a is the lattice constant, b is an integer that defines the number of air holes. (b) Sketch of the disorders for the radius and position of air holes. The dashed and full circles indicate holes of the regular and disordered structure respectively. (c) Band structure of the air-bridge W1 photonic crystal waveguide with slab thickness $d = 0.5a$, dielectric constant $\epsilon = 12$, air hole radius $r = 0.3a$, and $b = 10$. Band 1 (red) is the spatially even guided TE mode. Band 2 is the odd guided TE mode. Band 3 and 4 are modes at the boundaries of photonic crystal band gap. From Ref. [31].

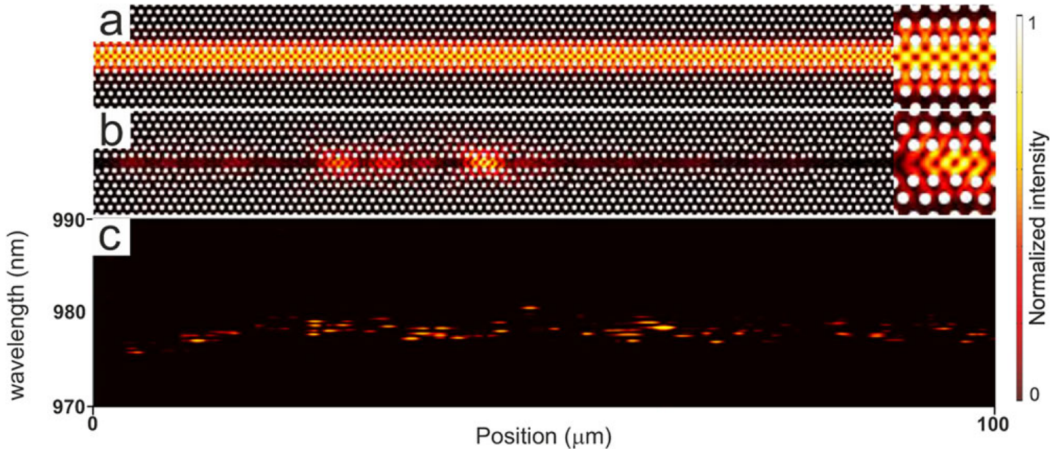

Figure 2.4: Finite-difference time-domain calculation of the electromagnetic-field intensity in an ideal (a) and in a disordered (b) W1 photonic crystal waveguide with a lattice constant $a = 260nm$ and a hole radius $0.29a$, calculated at the cutoff frequency of waveguide mode. The disordered waveguide is perturbed by $\sigma = 0.04a$. (c) Experimentally recorded high-power photoluminescence spectra collected while scanning a microscope objective along a photonic crystal waveguide with only intrinsic disorder ($\sigma = 0$). From Ref. [32].

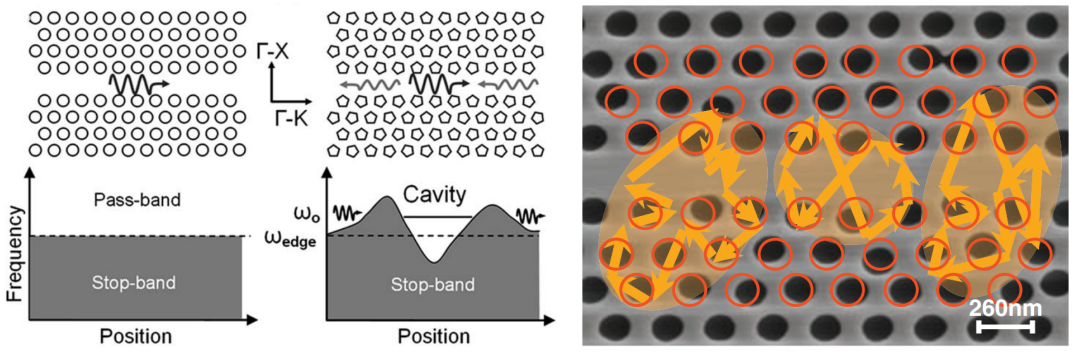

(a) (b)

Figure 2.5: Theories of Anderson localization in disordered photonic crystal waveguide. (a) Schematic of disorder induced fluctuations of the band edge (ω_{edge}), which create cavities where photons of certain frequencies (ω_0) are confined. From Ref. [33]. (b) Schematic of multiple scattering induced localization in a photonic crystal waveguide with 6% engineered disorder. The red circles represent the hole positions in an ideal structure without disorder. The orange arrows depict the wavevectors of localized modes. From Ref. [34].

The most investigated disorders in PhC waveguides are the variations of air hole's radius and the displacements of air hole's position, as shown in Figure 2.3(b). The roughness of slab surface and the deformations of air hole's shape are also common sources of disorder in photonic crystal waveguides. These are all ubiquitous imperfections that happen in practical fabrications, even for state-of-the-art technologies.

A large amount of researches on disordered photonic crystal waveguides focus on the W1 line-defect triangular lattice waveguide, since its band structure is typical and well-known. Figure 2.3(a) shows the physical structure of a W1 photonic crystal waveguide and Figure 2.3(c) shows its band structure. Band 1, the spatially even guided TE mode, is the main propagating mode in a W1 photonic crystal waveguide. Its highly dispersive curve leads to low group velocities near the lower edge of the band, and should reach zero-velocity in an ideal situation. However, in practical situations, this slow light regime is always disturbed by fabrication error induced disorders and cannot reach its theoretical limit.

In an ideal photonic crystal waveguide, the spatial profile of electromagnetic field in slow light regime should be periodic along the line-defect direction, obeying the Bloch wave behavior. Nevertheless, in a disordered photonic crystal waveguide, there will be random localization occurred along the waveguide, disturbing slow light transport, as shown in Figure 2.4. This phenomenon is called Anderson localization in photonic crystal waveguide.

The origin of Anderson localization is an interplay of order and disorder. There are two theories that are used to explain the cause of Anderson localization.

The first theory is illustrated in Figure 2.5(a). Disorders like the irregular

shapes of air holes will break the periodicity of photonic crystals and induce fluctuations of the guided mode's band edge in spatial domain along the line-defect direction. The fluctuations of the boundary between pass-band and stop-band create random cavities in the waveguide where photons of certain frequencies can penetrate through the barriers and resonate inside, leading to Anderson localization [33]. This explanation is vivid and easy to understand, but is limited to strong localization that happen at frequencies near the band edge.

The second and more general explanation is that disorders in photonic crystal waveguides can induce multiple scattering, which causes localized modes along the line defect [34], as displayed in Figure 2.5(b). Therefore, not only near-band-edge frequencies have sharp localization, but also frequencies well within the propagating regime of the guided band will show irregular amplitude fluctuations induced by disorder, which helps enhance the performance of our reconstructive spectrometer as discussed later.

To further understand Anderson localization, researchers proposed some parameters to quantify the features of Anderson localization. In this thesis we are going to look at two important parameters: the Lifshitz tail width and the localization length.

2.2.1 The Lifshitz tail

The Lifshitz tail in a photonic crystal waveguide is a spectral region around the band edge (cut-off frequency) where the energy densities from the waveguide show sharp peaks [36], as shown in Figure 2.6. These peaks are determined by Anderson localization, and the spectral width of the region where localized modes appear can be considered as the width of the Lifshitz tail which quantifies the amount of fabrication disorder in a photonic crystal waveguide [35]. The insets of Figure 2.6(c) shows the finite-difference time-domain (FDTD) simulation results of electromagnetic field intensity ensemble averaged over a total of 10 disordered photonic crystal waveguids vs wavelength, with $\sigma = 0.02a$, $\sigma = 0.04a$ and $\sigma = 0.06a$ [35]. The standard deviation refers to the displacements of air hole position. Due to the finite number of simulation samples, the sharp resonances are unevenly distributed and not fully converged, but nonetheless the width of the Lifshitz tail apparently increases with the amount of disorder.

From the same work, the width of the Lifshitz tail is measured experimentally for photonic crystal waveguides with different amount of engineered disorder. The test subjects are 100 μm long photonic crystal waveguides with lattice constant $a = 260$ nm, hole radius $r = 78$ nm, and slab thickness 150 µm. Multiple quantum dots (QDs) are embedded along the waveguide to excite the Anderson localized modes. The engineered disorders σ_e are displacements of air hole positions in the same way for the simulations in Figure 2.6. The worth noting observation here is the intrinsic disorder induced localization. Figure 2.7(a) shows the scanning-electron image of a photonic crystal waveguide with intrinsic irregular shapes and

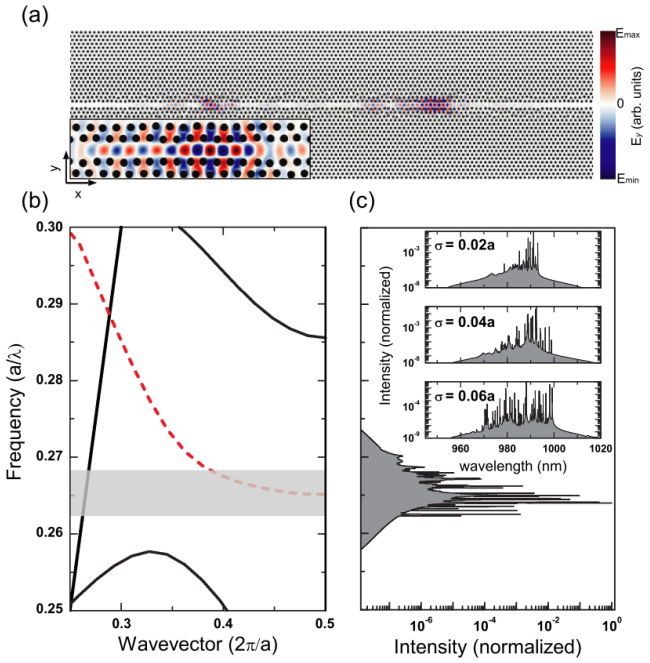

Figure 2.6: (a) Finite-difference time-domain calculation of electric field component of a W1 photonic crystal waveguide with the standard deviation of air hole position displacements $\sigma = 0.04a$. (b) Dispersion relation of an even-parity photonic crystal guided mode (dashed-red curve). The shaded region around the mode cutoff outlines the spectral region where Anderson localized modes appear determining the Lifshitz tail. (c) Calculated normalized electromagnetic field intensity ensemble averaged over 20 different positions along a single waveguide and a total of 10 disordered photonic crystal waveguides with $\sigma = 0.04a$. The insets show the shapes of Lifshitz tail at different amount of disorder. From Ref. [35].

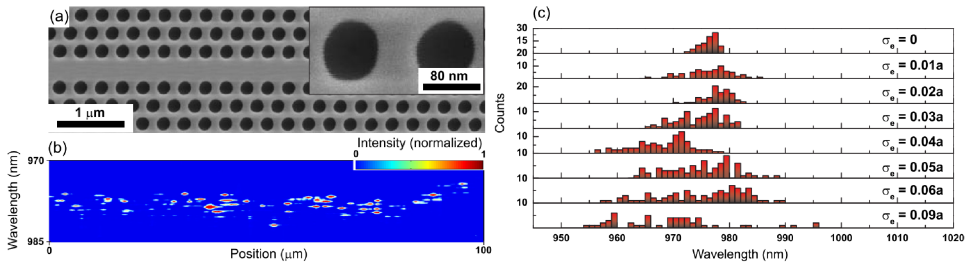

Figure 2.7: (a) Scanning-electron micrograph of a photonic crystal waveguide without engineered disorder. The inset illustrates that unavoidable irregular shapes and sizes of the holes are present in the samples. (b) Normalized high-power photoluminescence spectra collected while scanning a microscope objective along a photonic-crystal waveguide with only intrinsic disorder ($\sigma_e = 0$). The bright peaks that appear randomly along the waveguide and close to the waveguide mode cutoff correspond to Anderson localized modes. The spectral region where the modes appear defines the experimental Lifshitz tail. (c) Histogram of the spectral position of the Anderson-localized modes for different amounts of engineered disorder σ_e. The width of the Lifshitz tail increases with the amount of disorder. From Ref. [35].

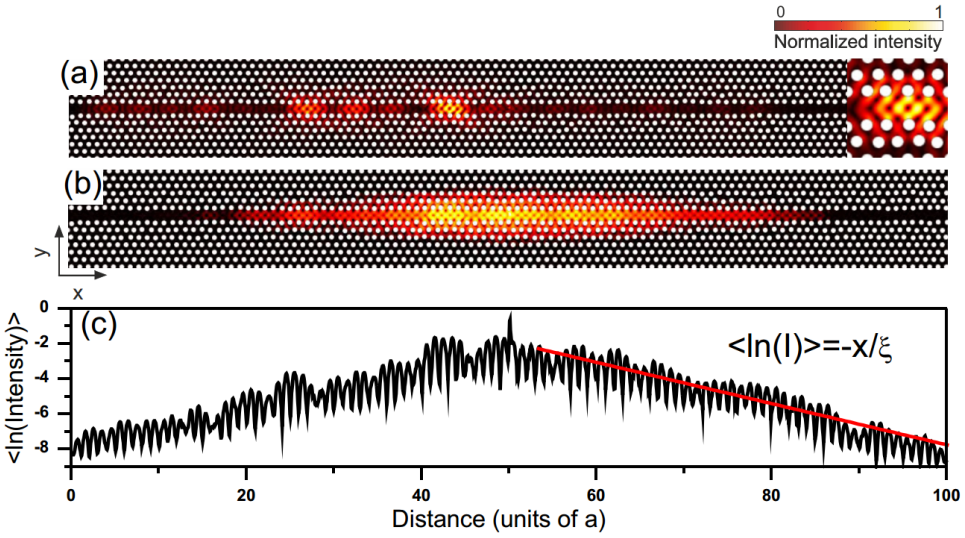

Figure 2.8: Localization length in disordered photonic crystal waveguides. (a) Steady-state electromagnetic-field intensity (normalized) emitted from a dipole at $\omega = 0.266a/\lambda$ placed at the center of a disordered photonic crystal waveguide perturbed by $\sigma = 0.04a$. The source frequency is near the cut-off frequency of the unperturbed waveguide mode. (b) Ensemble average over 10 different disorder configurations with $\omega = 0.266a/\lambda$ and $\sigma = 0.04a$. (c) Ensemble-averaged electromagnetic-field intensity profile along the waveguide direction. The localization length can be extracted from the slope of the exponential decay. From Ref. [37].

sizes of air holes, which are enough to induce clear Anderson localized modes within a narrow spectral range around the cut-off wavelength ($\lambda = 978$ nm), as shown in Figure 2.7(b). Similar to Figure 2.4(c), the width of the Lifshitz tail can be extracted from these high-power photoluminescence spectra along the waveguide, by counting the number of Anderson localized modes at each wavelength. The histogram of the Anderson localized modes spectral positions for different amount of engineered disorder are displayed in Figure 2.7(c). It demonstrates that the Lifshitz tail broadens spectrally when increasing the amount of disorder, matched to simulation results. In addition, even the photonic crystal waveguide with only intrinsic disorder ($\sigma_e = 0$) shows considerable counts of Anderson localized modes and a relatively wide Lifshitz tail, indicating the potential applications of intrinsic disorders.

2.2.2 The localization length

The localization length is another statistical parameter for Anderson localization. Although the Anderson localized modes are considered as random events that their positions in the photonic crystal waveguide are unpredictable, after ensemble averaging over many configurations of disorder, the intensity pattern envelope shows an exponential damping from the position of the source [37], as shown in Figure 2.8, in which a dipole source is placed at the center of a disordered photonic crystal waveguide.

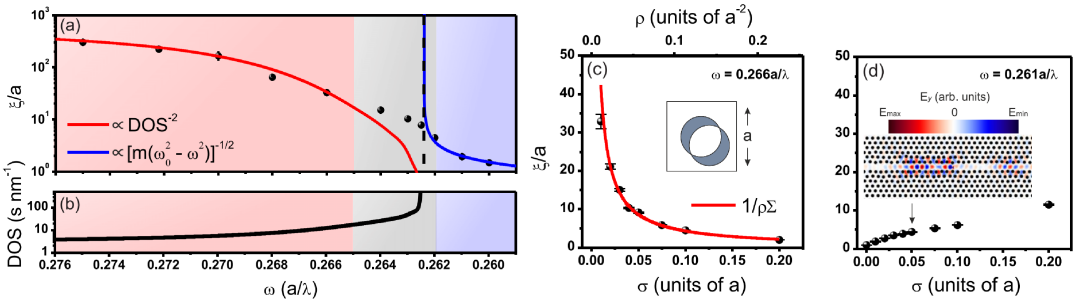

Figure 2.9: Two mechanisms of disorder induced localization. (a) Localization length calculated in a photonic-crystal waveguide with air hole radius $0.29a$ perturbed by $\sigma = 0.01a$ (black dots). The dashed line pinpoints the cut-off frequency of the propagating Bloch mode in the ideal structure. In the band region of a propagating waveguide mode, the localization length ξ is proportional to DOS^{-2}, represented by the red line, while in the band gap region ξ is proportional to m^{-2}, represented by the blue line, where DOS is the density of states and m is the effective photon mass in photonic crystal. (b) The black line plots the corresponding DOS of a perfect photonic crystal waveguide. (c) The localization length ξ vs disorder σ at $\omega = 0.266a/\lambda$ (inside band). (d) The localization length ξ vs disorder σ at $\omega = 0.261a/\lambda$ (inside band gap). From Ref. [37].

The localization length is a parameter that describes the decay rate, and can be expressed as

$$< \ln(I) >= -x/\xi \tag{2.1}$$

where "<>" means ensemble average, I is the energy intensity dependent on the position, x is the distance from the source, and ξ is the localization length, as shown in Figure 2.8(c).

The localization length is a very important parameter that indicates the possibility of the occurrence of Anderson localization. If the length of the photonic crystal waveguide is much longer than the localization length of a wavelength, then Anderson localized modes are highly possible to happen at this wavelength. On the contrary, if the length of the waveguide is much shorter than the localization length, Anderson localization at this wavelength will be suppressed. Therefore, for nanostructures that intend to avoid Anderson localization, one strategy is to build structures with dimensions much smaller than the localization lengths.

What we are interested here is how the localization length varies with the wavelength and amount of disorder. García et al. has presented a detailed numerical analysis of two mechanisms that determines the localization length in a disordered photonic crystal waveguide [37]. Figure 2.9(a) plots the dispersion of localization length ξ calculated from FDTD simulations. The simulation subject is a triangular lattice W1 photonic crystal waveguide with a lattice constant $a = 260$ nm and an air hole radius $r = 0.29a$. An effective refractive index of $n = 2.76$ is used to represent the 150-nm-thick photonic crystal slab in two-dimensinal simulations. Disorders are introduced by displacing the positions of air holes with a standard deviation

$\sigma = 0.01a$. Two analytical models describing the scaling of ξ vs ω are plotted as red line and blue line, while the calculated results are displayed by black dots and the cut-off frequency is plotted as dashed line. In the propagating regime (red-shaded area), ξ is proportional to DOS^{-2}, where $\mathrm{DOS} = (1/\pi)\partial k/\partial\omega$ is the density of states of the propagating mode [38], while in the evanescent regime (blue-shaded area) ξ is proportional to $[m({\omega_0}^2 - \omega^2)]^{-2}$, where $m = (\partial^2\omega/\partial k^2)^{-1}$ is the effective photon mass in the photonic crystal, which is obtained as the inverse of the band curvature of the unperturbed mode, ω_0 and ω are the cut-off frequency if the unperturbed and perturbed structure respectively. Furthermore, a crossover region (gray-shaded area) connects the two regimes. As mentioned earlier in Section 2.2, in the propagating regime Anderson localization is mainly caused by multiple scattering, while in the crossover regime and evanescent regime around the ideal cut-off frequency the fluctuations of band edge creates random barriers that confine light. The two mechanisms in Figure 2.9(a) help us have better understanding on Anderson localization, and reveal the tendency that localization length decreases with input frequency.

García et al. has further investigated the relationship between the localization length and amount of disorder [37]. The simulations are carried out at two different frequencies, one in the propagating regime $\omega = 0.266a/\lambda$, plotted in Figure 2.9(c), and the other one in the evanescent regime $\omega = 0.261a/\lambda$, plotted in Figure 2.9(d). The dependence of localization length with disorder is opposite at these two frequencies: it decreases in the propagating region while it increases in the evanescent region. The former can be explained as the increase of the effective scattering area (Figure 2.9(c) inset, shaded area) enlarges the density of scatters ρ, while $\xi \propto 1/\rho\Sigma$ where Σ is the scattering cross section proportional to DOS^2. The latter can be considered as the additional disorders increase the curvature of band edge and the effective photon mass m is reduced.

2.2.3 Summary of Anderson localization

The unavoidable fabrication errors in photonic crystal waveguide can induce Anderson localization, either by multiple scattering or random cavities caused by band edge fluctuations. The spectral range of Anderson localization is measured by the Lifshitz tail width, which increases with the amount of disorder. The spatial position range of Anderson localization is quantified by the localization length, which decreases as the input light moves to longer wavelengths. When the amount of disorder becomes larger, the localization length dramatically decrease in the propagating region while it slightly increases in the evanescent region.

The numerical simulation work by Savona presents a good overview of how disorder affects the band structure of a W1 photonic crystal waveguide [31]. The simulations use an air-bridge photonic crystal waveguide with configuration $d = 0.5a$, $r = 0.3a$, $b = 10$, and effective slab dielectric constant $\bar{\epsilon}_2 = 8.77$ for two-dimensional simulation. Note that the actual physical dimension of the structure is unnecessary for simulation parameters

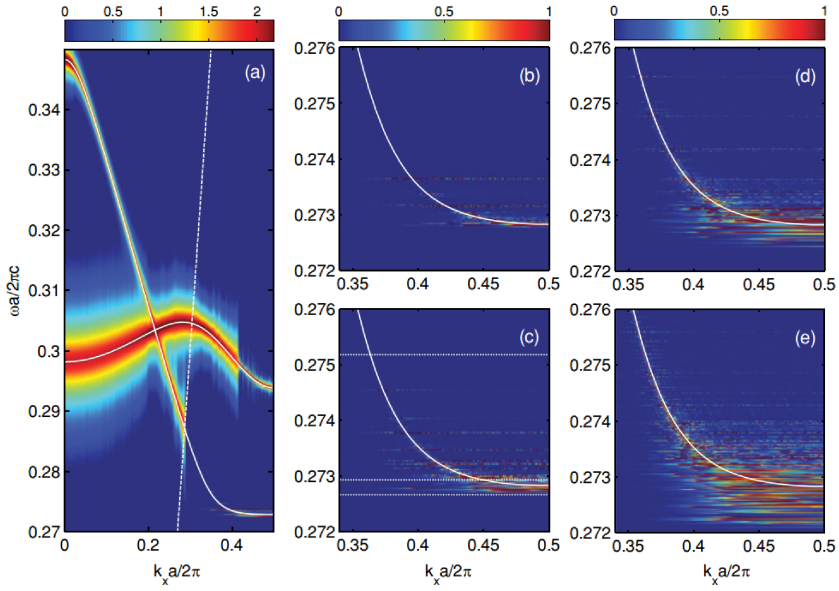

Figure 2.10: Spectral density of the disordered W1 photonic crystal waveguide, visualizing the spectral contribution of localized modes. (a) Overall view of spectral density around Band 1 and 2 mentioned in Figure 2.3, plotted on a $\log_{10}$ color scale for $\sigma = 0.002a$. The dotted line is the boundary of the light cone. (b)-(e) Detailed view of the spectral density at the lower edge of Band 1 for $\sigma = 0.001a$, $\sigma = 0.002a$, $\sigma = 0.004a$, $\sigma = 0.008a$, respectively. From Ref. [31].

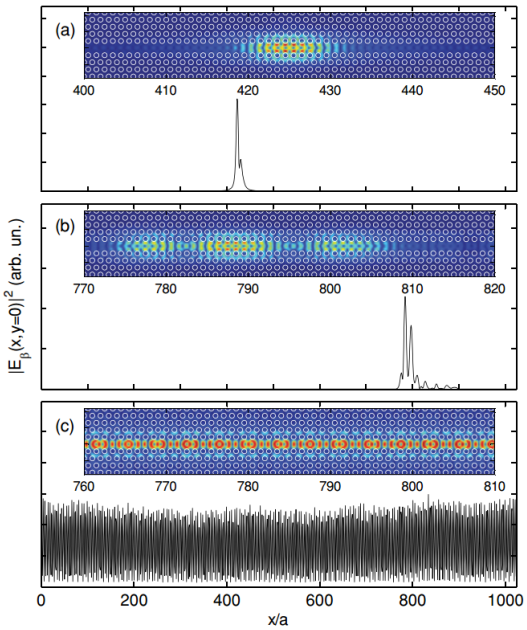

Figure 2.11: (a)-(c) Electric field spatial profile of three selected eigenmodes computed for $\sigma = 0.002a$, at frequencies $\omega a/2\pi c = 0.27267$, 0.27283, and 0.27518, respectively [indicated by horizontal dotted lines in Figure 2.10(c)]. The main panels display the field intensity computed at the center of each elementary cell, while insets show the full field profile for selected portions of the W1 waveguide. From Ref. [31].

as people are used to express variables in a ratio way, like frequency ω is specified in units of $2\pi c/a$, while wave vector k is specified in units of $2\pi/a$. The merit of using dimensionless units is that the band structure of different nanostructures can be easily compared. If the actual physical scale is needed, it can be acquired by just bringing the value of lattice constant a.

The disorders are introduced by a Gaussian fluctuation of both air hole radii r_m and positions (x_m, y_m), where m traverses all holes of the photonic crystal waveguide. The standard deviation is set as $\sigma_r = \sigma_x = \sigma_y = \sigma$, which ranges from $0.001a$ to $0.008a$, corresponding to state-of-the-art fabrications. Figure 2.10(b)-(e) shows the calculated spectral density around the guided band, for $\sigma = 0.001a$, $0.002a$, $0.004a$, and $0.008a$, respectively. It can be clearly observed that the width of the Lifshitz tail increases with the disorder level, and these Anderson localized modes extend along k direction as σ is increased.

The electric field profiles of three selected modes (indicated by three dotted lines in Figure 2.10(c)) of a realization with $\sigma = 0.002a$ are plotted in Figure 2.11(a)-(c) respectively. The main plot in each panel represents the value of the field intensity at the center of the waveguide over the full length of the simulated structure, while the insets show the close look of electric field profile for selected representative regions in the waveguide. Figure 2.11(a) shows the mode lying below the band edge and is localized over a tight distance. Figure 2.11(b) shows the mode slightly above the band edge, with a less localized three-lobe profile over a larger distance. Such mode with several lobes and an overall envelope with exponentially decaying tails is a typical character for Anderson localized states. As mentioned in Section 2.2.2, the localization length increases with frequency, meaning the localization length is in an ascending order for (a)-(c). Figure 2.11(c) shows the mode well within the propagating regime and is delocalized over the whole length of the simulated waveguide while still showing irregular amplitude fluctuations induced by disorder. This is due to the localization length at this frequency is much longer than the simulation length.

As shown in Figure 2.11, the disordered photonic crystal waveguide has different localization profiles for different wavelengths, even wavelength in propagating region shows signature profile induced by disorder. We believe these unique localization profiles can be utilized as characteristic patterns of a reconstructive spectrometer, and proposed a chirped photonic crystal waveguide structure, which will be introduced in next section.

2.3 Chirped structure and reconstruction algorithm

When the waveguide width of a photonic crystal waveguide is slightly decreased, the band edge of TE propagating even mode inside the photonic crystal band gap will slightly shift towards the shorter wavelength side, as shown in Figure 2.12(b).

The photonic crystal waveguide based reconstructive spectrometer introduced in this work consists of a chirped photonic crystal waveguide, as shown in in Figure 2.12(a). Triangular lattice photonic crystal waveguide

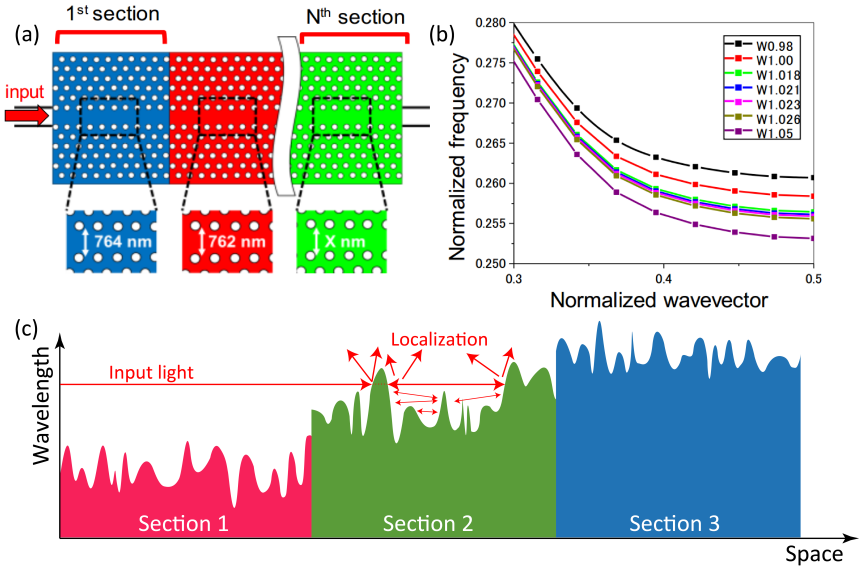

Figure 2.12: (a) Schematic of the chirped PhC waveguide structure. A camera monitors the energy intensity profiles from the top of the slab. (b) Band structure of the guided mode for different PhC waveguide widths. The band edge shifts to larger frequencies when the PhC waveguide width increases. [(a)-(b) are from Ref [39]] (c) Schematic of Anderson localization in a chirped waveguide. The colored area represents the stop-band, and the white area represents the pass-band.

sections with gently decreasing waveguide widths are connected in a straight line [28].

If the chirped photonic crystal waveguide is perfect with zero fabrication error, then its band structure will remain consistent inside each section. The band edges in the spatial domain will be flat lines connected in a stairs shape. There will be some strong backscatterings for wavelengths that are forbidden to propagate in the next section at the junctions of neighboring sections, which can be used to group input wavelengths that are exclusive to this PhC waveguide section. However, the further distinction of wavelengths is difficult due to their highly linear correlated energy density profiles.

In practical fabrications, there are always fabrication errors happening to the photonic crystal structures. The center positions and shapes of the air holes may experience some unpredictable disturbances. The periodicity of the photonic crystal waveguide is broken, and the band edges in the spatial domain will fluctuate along the direction of light propagation. Some random optical cavities are generated and cause Anderson localization inside the line defect of the PhC waveguide, as shown in Figure 2.12(c). Because of fabrication errors, the scattered light that escapes from the total internal reflection condition increases, especially at the optical cavities. By collecting the scattered light using an infrared camera and macro lens, we can obtain near-field images that contain the localization profiles of input wavelengths. The wavelength-sensitive localized modes add great information to the energy intensity profiles that help reconstruct the input spectrum.

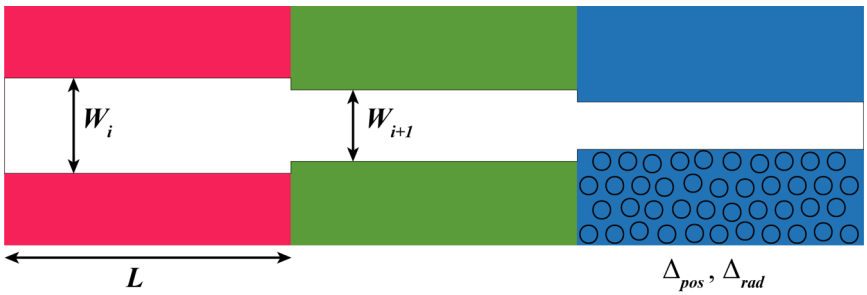

Figure 2.13: The geometry parameter variables covered in this work: the length of each section L, the reduction rate of waveguide width $W_{i+1} - W_i$, and the disorder level of air holes $\Delta_{pos}, \Delta_{rad}$.

Here introduce the details about the reconstruction algorithm of this spectrometer design.

After the fabrication of each chirped photonic crystal waveguide spectrometer chip, the first step is calibration. Inject a single-wavelength laser into the PhC waveguide and take near-filed images of its localization pattern from the top of chip by camera when the system reaches its steady state. Multiple images are taken and averaged to suppress white noise and the brightness information of pixels around the line defect is recorded as a 2-dimensional array, which is further summed in the transverse direction of the waveguide to a 1-dimensional column array, such as $\vec{I_{\lambda_q}} = \left\{ i_p^{(\lambda_q)} \right\}$, where p refers to the longitudinal spatial position. This 1-dimensional column array contains the calibration data of the corresponding single-wavelength input λ_q. Change the input wavelength and repeat the procedure. The scan range of wavelengths should cover the working wavelengths of the spectrometer, and the scan step size should be set small enough as it determines the theoretical resolution limit of the reconstruction algorithm. When the single-wavelength scanning is completed, we place the 1-dimensional columns in ascending wavelength order to get a 2-dimensional transfer matrix $\boldsymbol{T}$ that represents the spectral-to-spatial mapping of the device.

$$\boldsymbol{T} = \left[\vec{I_{\lambda_1}} \ \vec{I_{\lambda_2}} \ \cdots \ \vec{I_{\lambda_3}} \right] = \left\{ i_{p,\lambda_q} \right\} \tag{2.2}$$

We use this matrix $\boldsymbol{T}$ as calibration data. For a single wavelength input λ, the relationship between the input spectrum $\vec{S}$ and the measured spatial energy density profile $\vec{I_\lambda}$ can be expressed as

$$\vec{S} = \boldsymbol{T}^{-1} \vec{I_\lambda} \tag{2.3}$$

This relationship is valid even for multi-wavelength input because the spatial energy density profiles for different wavelengths can be linearly combined, as we will discuss later. Solving this linear equation is the core of the reconstruction algorithm.

In practical implementations, the linear equation is always disturbed by measurement inaccuracies and experimental noise. We define a cost given as

$$C(\vec{S}) = \|\vec{I_\lambda} - \boldsymbol{T}\vec{S}\|_2 + \|\vec{S}\|_1 \tag{2.4}$$

The best possible solution $\vec{S}$ is found by minimizing the cost $C(\vec{S})$. We apply the fast iterative shrinkage-thresholding algorithm (FISTA) [40] to find the solution.

A published work from our group presented a prototype design of such a PhC waveguide structure, with a test chip fabricated. A wavelength range from 1596.6 to 1604.4 nm with 0.2-nm resolution is recorded [28].

In this work, the relationship between geometry parameters of the chirped PhC waveguide and performance as a spectrometer is further investigated. As shown in Figure 2.13, we focus on three topics: the length of each section, the reduction rate of waveguide width, and the disorder level of air holes.

Chapter 3

Simulation Method and Setups

3.1 FDTD method

As we mentioned in the previous chapter, the photonic crystal waveguide structure that we are interested in features randomly distributed disorders. Due to the existence of disorders for both the radius and center location of the airholes, the whole structure becomes asymmetric and aperiodic. Simulation methods like Beam Propagation Method (BPM) and Finite Element Method (FEM) are not effective for such structures. So we decided to use a Finite-Difference Time-Domain (FDTD) method to calculate the steady-state

3.2 MEEP simulation setups

The simulation tool we used is MEEP [41], an open-source software package for electromagnetics simulation via the Finite-Difference Time-Domain (FDTD) method.

A Python script "`phcwg01.py`" is created to define default simulation parameters and Python functions that are used for MEEP simulations. A control script "`phcwg_master.py`" that imports "`phcwg01.py`" is edited every time to twist simulation parameters and run MEEP simulations.

In "`phcwg01.py`", a class "`PhC`" is defined as a container to store all constant objects, as all physical parameters that determine the simulated PhC waveguide structure and other constant parameters are defined as data attributes of an instance object of the class "`PhC`". The following are definitions of some essential attributes for the simulation setup.

`PhC.n`: the material refractive index for photonic crystal waveguide. The default value is 2.788, calculated as the effective refractive index [42] of a silicon slab with 0.2 μm thickness sandwiched between silica coatings and photonic crystal holes filled by silica.

`PhC.nb`: the background refractive index, which refers to the refractive index of air holes of the photonic crystal. The default background material is silica with a refractive index of 1.444.

`PhC.a`: the lattice constant a of the photonic crystal. The default value is 0.42 μm.

`PhC.r`: the air hole radius of the photonic crystal. The default value is 0.12 μm.

`PhC.periods`: the total length of the PhC waveguide in units of the lattice constant a (the period of photonic crystal). This is one of the main variables that get twisted in this work since we are interested in the optimal length of a single section in the chirped PhC waveguide structure.

`PhC.w_wg`: the waveguide width of the PhC waveguide, defined as the distance between photonic crystal air hole rows on the two sides of the line defect. If it is a multiple-section structure, then `PhC.w_wg` is the waveguide width of the first section. The default value refers to a W1 PhC waveguide, which is created by simply removing a single row of air holes in the triangular lattice without any shift to the remaining air holes' locations.

`PhC.section`: the number of sections in the chirped PhC waveguide structure. The sections are evenly separated along the PhC waveguide, with each section taking a length of `PhC.periods/PhC.section`.

`PhC.shrink_rate`: the reduction rate of the chirped PhC waveguide's width, in units of percentage. The waveguide width of each chirped PhC waveguide section will decrease by `PhC.shrink_rate*PhC.w_wg` from the previous section. For example, if `PhC.shrink_rate` = 0.01, while `PhC.w_wg` is the default value, the first section will be a W1 PhC waveguide, the second section will be a W0.99 PhC waveguide, the third section will be a W0.98 PhC waveguide, and so on.

`PhC.Sigma_d`: the standard deviation σ_d of the air hole displacement, which is assumed to be a normal distribution with an expectation of zero. The default value is 0.002 μm. This is in the same order as the practical fabrication error on the prototype chip.

`PhC.Sigma_r`: the standard deviation σ_r of the air hole radius error, which is assumed to be a normal distribution with an expectation of zero. The default value is 0.002 μm.

`PhC.dpml`: the depth of the PML layer surrounding the simulation cell. The default value is 2 times the lattice constant.

Considering the scale of our device, especially the length of the PhC waveguide, we chose a 2-dimensional FDTD method to simulate the localization patterns of the structure rather than a full 3-dimensional FDTD calculation, since the simulation of a full-length chirped PhC waveguide spectrometer is inefficient and impractical. The computing resources we have can support a maximum PhC waveguide length of 240 periods within the tolerance of computation time. To balance the simulation time and precision, a grid size of 0.028 μm is used for 2D FDTD simulation. Thanks to MEEP's support for subpixel smoothing, the effect of nanometer-scale disorders can still be revealed in simulations to a certain extent.

To suppress the cost of simulation time, the width of the simulation domain is limited to only include 5 rows of photonic crystal holes on both sides of the line defect.

To obtain the localization patterns of the device at different input wavelengths, we use a short-duration broad-bandwidth pulse to excite the device and compute the Fourier transform of the fields as the steady-state field responses.

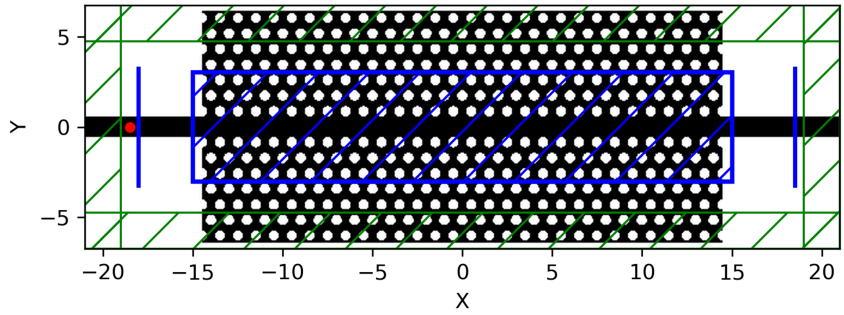

Figure 3.1: Setup for 2D-FDTD simulation. Red dot: Guassian point source. Blue shaded area: spatial energy density monitor. Blue line: power flux monitor. Green shaded area: perfectly matched layer (PML).

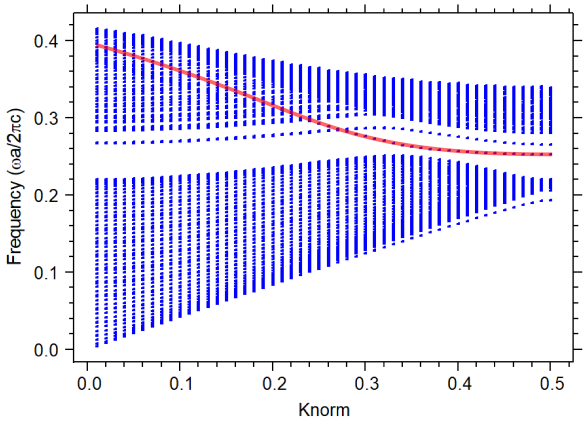

Figure 3.2: Band structure calculated for the ideal W1 PhC waveguide with default parameters. The TE guided even mode is shown in red curve and its band edge frequency is $0.252(2\pi c/a)$, which is equivalent to a wavelength of 1.667 µm.

A Gaussian point source is placed inside the input rectangular waveguide, which is equivalently a slab waveguide in 2-dimensional FDTD simulation. Power flux monitors are placed on both the input and output sides of the PhC waveguide to measure its propagation loss.

Considering the band-edge wavelength of a W1 PhC waveguide is at about 1.667 µm, and the shift of band-edge towards shorter wavelengths due to the reduction of waveguide width in chirped structure, the recording wavelength range is decided to be from 1.55 µm to 1.7 µm, at a step size of 0.001 µm. The choice of step size is a compromise to time-consuming but should be small enough to reveal the wavelength sensitivity of the spectrometer.

The monitoring area of energy density is shown as the shaded area, which includes about 3 rows of photonic crystal air holes on both sides of the line defect. For the near-band-edge wavelengths that we are interested in, most energy is constrained inside the line defect area, so the monitoring area is sufficient to record almost every useful information we want.

The simulation is stopped when the total energy in the simulation domain is decayed by 0.001 from its maximum recorded value.

Chapter 4

Simulation Results and Analyses

4.1 Performance analysis method

When the 2D FDTD simulation is finished, the 2-dimensional spatial profiles of the energy intensity for wavelengths are acquired. We use these 2D FDTD simulation results to approximate the near-filed images of localization patterns observed in practical experiments mentioned in Section 2.3. An example of localization pattern in a $40a$ long disordered PhC waveguide at $\lambda = 1.667$ µm is shown in Fig 4.1(b), and its converted 1-dimensional data is plotted in Fig 4.1(c).

Following the same calibration procedure as practical experiments, the 1-dimensional data are sorted as columns by the wavelength order to produce the transfer matrix $\boldsymbol{T}$, which represents the spectral-to-spatial mapping of the structure. An example of the spectral-to-spatial mapping of an $80a$ long disordered PhC waveguide is plotted in Figure 4.2(a). The small lobes observed in vertical direction are expected behavior of Bloch wave, with a periodicity equal to the lattice constant a.

The spectral-to-spatial mapping matrix is a key for performance analysis as we can calculate wavelength-dependent spectral resolutions from it.

4.1.1 Spectral resolution

The most important numerical value to evaluate the performance of this device is the spectral resolution. We use the Pearson correlation coefficient [43] to define the spectral resolution function $\Theta(\Delta\lambda, \lambda_q)$, which represents the similarity between the energy intensity profile I_{λ_q} of the center wavelength λ and the energy intensity profile $I_{\lambda_q+\Delta\lambda_q}$ of a near-by wavelength $\lambda + \Delta\lambda_q$.

$$\begin{aligned}\Theta(\Delta\lambda, \lambda_q) &= \frac{cov(I_{\lambda_q}, I_{\lambda_q+\Delta\lambda_q})}{\sigma(I_{\lambda_q})\sigma(I_{\lambda_q+\Delta\lambda_q})} \\ &= \frac{\sum_{p=1}^{m}(i_{p,\lambda_q} - \overline{I_{\lambda_q}})(i_{p,\lambda_q+\Delta\lambda} - \overline{I_{\lambda_q+\Delta\lambda_q}})}{\sqrt{\sum_{p=1}^{m}(i_{p,\lambda_q} - \overline{I_{\lambda_q}})^2}\sqrt{\sum_{p=1}^{m}(i_{p,\lambda_q+\Delta\lambda} - \overline{I_{\lambda_q+\Delta\lambda_q}})^2}}\end{aligned} \tag{4.1}$$

where $cov(I_{\lambda_q}, I_{\lambda_q+\Delta\lambda_q})$ is the covariance, $\sigma(I_{\lambda_q})$ and $\sigma(I_{\lambda_q+\Delta\lambda_q})$ are the standard deviations, $\overline{I_{\lambda_q}}$ and $\overline{I_{\lambda_q+\Delta\lambda_q}}$ are the means of I_{λ_q} and $I_{\lambda_q+\Delta\lambda_q}$. As

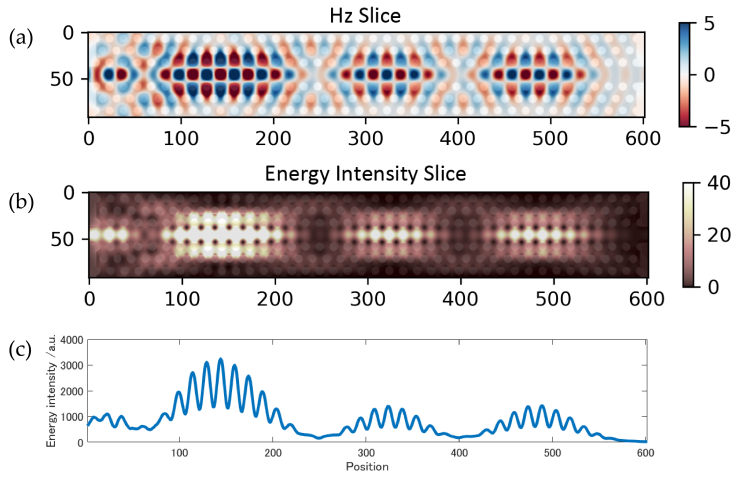

Figure 4.1: (a) H_z field slice and (b) energy intensity slice of a $40a$ long disordered PhC waveguide at $\lambda = 1.667$ µm. (c) Convert the 2-dimensional energy intensity slice to a 1-dimensional data by summing up the vertical direction intensities in (b).

mentioned in Section 2.3, I_{λ_q} is a 1-dimensional column array $I_{\lambda_q} = \left\{ i_p^{(\lambda_q)} \right\}$ that maps to the spatial position (pixel position) p, so it is a collection of variables and we can calculate the mean, standard deviation and covariance with $I_{\lambda_q+\Delta\lambda_q}$.

The Pearson correlation coefficient measures the linear correlation between two sets of data. Its value lies in the range from 1 to -1, where 1 represents perfect correlation and -1 represents perfect anti-correlation. In our case, $\Theta\left(\Delta\lambda,\ \lambda_q\right)$ has its maximum value 1 when $\Delta\lambda = 0$, and decreases with increasing $|\Delta\lambda|$. When $|\Delta\lambda|$ is large enough, the linear relationship between energy intensity profiles of the wavelength λ_q and $\lambda_q + \Delta\lambda$ becomes almost zero, which means their shapes are different enough and can be easily distinguished, with a positive or negative near-zero $\Theta\left(\Delta\lambda,\ \lambda_q\right)$ value. Since our purpose is to design a high-resolution spectrometer, the correlation coefficient at a small $|\Delta\lambda|$ is what we are interested in, which should be close to 1.

The conventional definition of the resolution of a spectrometer is the smallest distance $|\Delta\lambda|$ between two input wavelength peaks at which they can still be resolved as separate. To estimate the spectral resolution from the Pearson correlation coefficients, we set up a criterion value. For a center wavelength λ_q, if $\Theta\left(\Delta\lambda,\ \lambda_q\right)$ is above the criterion value, then the energy intensity profiles I_{λ_q} and $I_{\lambda_q+\Delta\lambda_q}$ are too similar to be accurately distinguished. If for positive $\Delta\lambda$, correlation coefficient $\Theta\left(\Delta\lambda,\ \lambda_q\right)$ is below the criterion value when $|\Delta\lambda| > res_{\mathrm{p}}$, and for negative $\Delta\lambda$, correlation coefficient $\Theta\left(\Delta\lambda,\ \lambda_q\right)$ is below the criterion value when $|\Delta\lambda| > res_{\mathrm{n}}$, then one half of the sum of smallest possible positive res_{p} and smallest possible positive res_{n} is the spectral resolution for this center wavelength λ_q. In this way, we can obtain individual spectral resolution $res = (res_{\mathrm{p}} + res_{\mathrm{n}})/2$ for each wavelength.

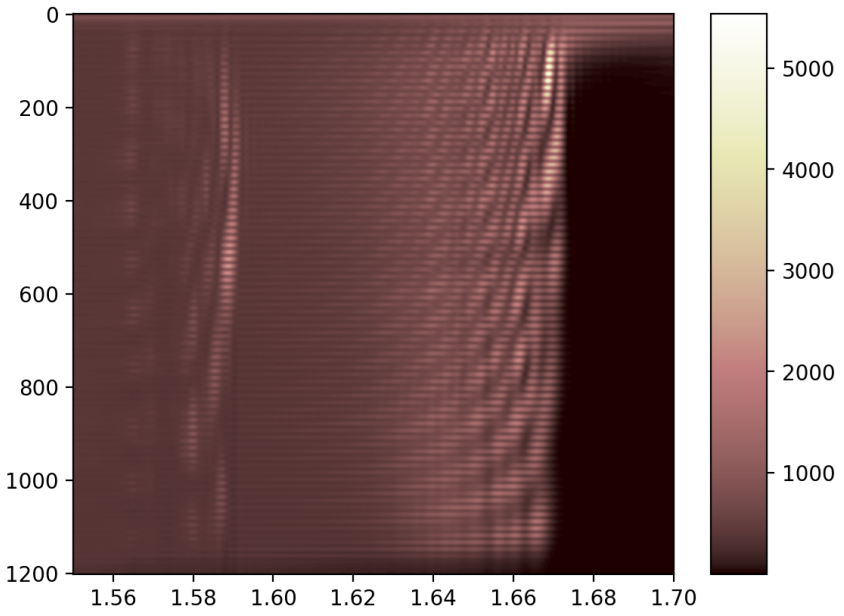

(a)

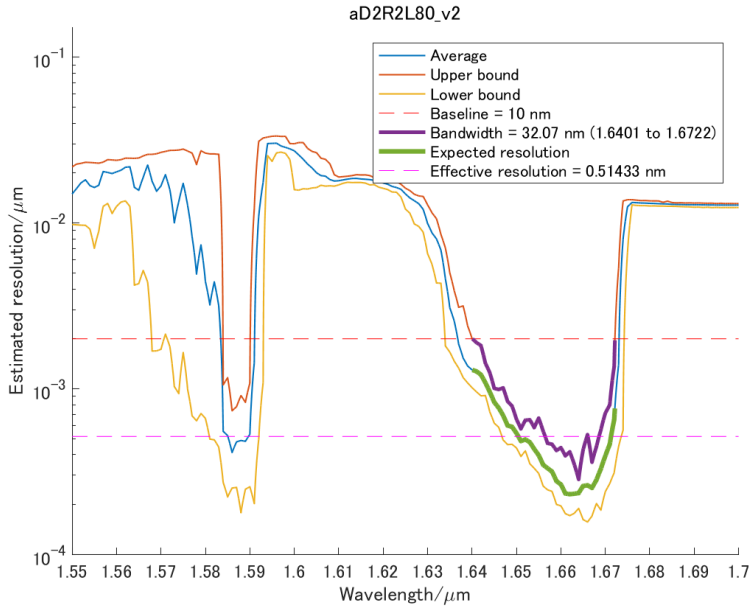

(b)

Figure 4.2: (a) The spectral-to-spatial mapping of an 80a long disordered PhC waveguide. The horizontal axis refers to the wavelength and the vertical axis refers to the pixel location. (b) The ensemble average of estimated resolutions for an 80a long W1 PhC waveguide. The horizontal axis is the wavelength and the vertical axis is resolution in log scale. The green curve shows the expected operating resolutions that are used to calculate the effective averaged resolution.

In this simulation work, we use a conservative criterion value of 0.9 to estimate the resolution at each recorded wavelength. The practical experiment data from previous works suggests that an even higher criterion value is possible. However, due to the simulation precision being limited on grid size, wavelength sampling rate, and PhC waveguide length, the resolutions in this simulation work are expected to downgrade. The criterion value of 0.9 is an appropriate choice to quantitatively estimate the spectral resolution of the spectrometer from simulation results.

4.1.2 Effective bandwidth and effective averaged resolution

The estimated resolutions of an $80a$ long single section W1 PhC waveguide are shown in Figure 4.2(b). In this figure, the line "Average" is the ensemble average of estimated resolutions over 16 individual PhC waveguide sample realizations, each sample with randomly generated fabrication errors.

Note that all simulation results in this thesis use 10% truncated means that discard the lowest 10% and the highest 10% spectral resolution of a wavelength. So the estimated resolutions of an $80a$ long disordered PhC waveguide mentioned above are actually statistical results generated from 20 individual runs. Due to the probability distribution of resolutions and limited number of simulated samples (10 or 20 runs mostly), by truncating some outliers we can get a more converged central tendency of data. In rest of this thesis, we will use total number of simulated samples instead of the number after truncation.

There are some strong localizations around the band-edge wavelength 1.667 μm observed in Figure 4.2(a), which contribute to the small spectral resolutions shown as a relatively deep and broad valley in the estimated resolution curve of Figure 4.2(b). The wavelengths inside this valley are the designed operating wavelengths of the spectrometer that we are interested in.

To quantitatively evaluate the operating wavelength range of the spectrometer, we define the operating wavelength range as a set where all wavelengths inside are guaranteed to have resolutions better than a baseline, which is 0.002 μm in this work. The judgement of operating wavelength range should consider the worst-case resolutions rather than the ensemble average, so we plot the line "Upper bound" and "Lower bound" in Figure 4.2(b) to show the fluctuation range of the spectral resolution at each wavelength. We consider that a wavelength is inside the operating range of the spectrometer if its "Upper Bound" of estimated resolution is below the baseline, so that all wavelengths inside the effective band are guaranteed to have resolutions better than 0.002 μm.

The bandwidth of the operating wavelength range is defined as effective bandwidth (bandwidth of the purple curve in Figure 4.2(b)), and the mean of "Average" resolution within the operating wavelength range is defined as the effective averaged resolution (mean of resolutions of the green curve in

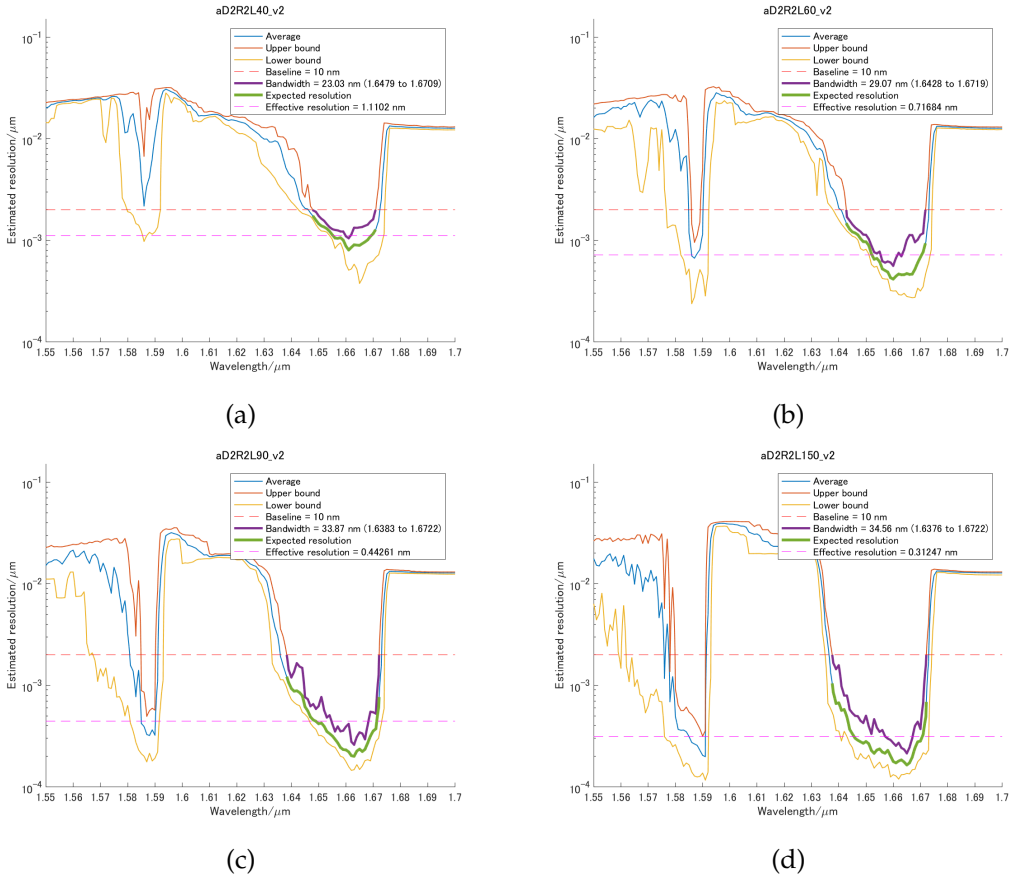

Figure 4.3: (a)-(d) Estimated resolutions for section lengths of 40a, 60a, 90a and 150a.

Figure 4.2(b)). The effective bandwidth and effective averaged resolution are two important numerical indicators of the spectrometer's performance.

Besides the localization patterns around the band-edge wavelength 1.667 μm, some localizations also happened around the 1.59 μm in Figure 4.2(a), which are odd mode localizations caused by the broken symmetry of disordered photonic crystal airholes. These odd mode localizations are relatively narrow-band, so they are not our primary focuses, though in a long broad-band chirped structure they are expected to provide additional information that helps improve the resolution of spectrometer when the odd mode localization bands in preceded sections happen simultaneously with even mode localization bands in succeeded sections.

4.2 Varying the section length of the PhC waveguide

In this section, we investigate how the length of a single section in a chirped photonic crystal (PhC) waveguide affects its performance as a spectrometer.

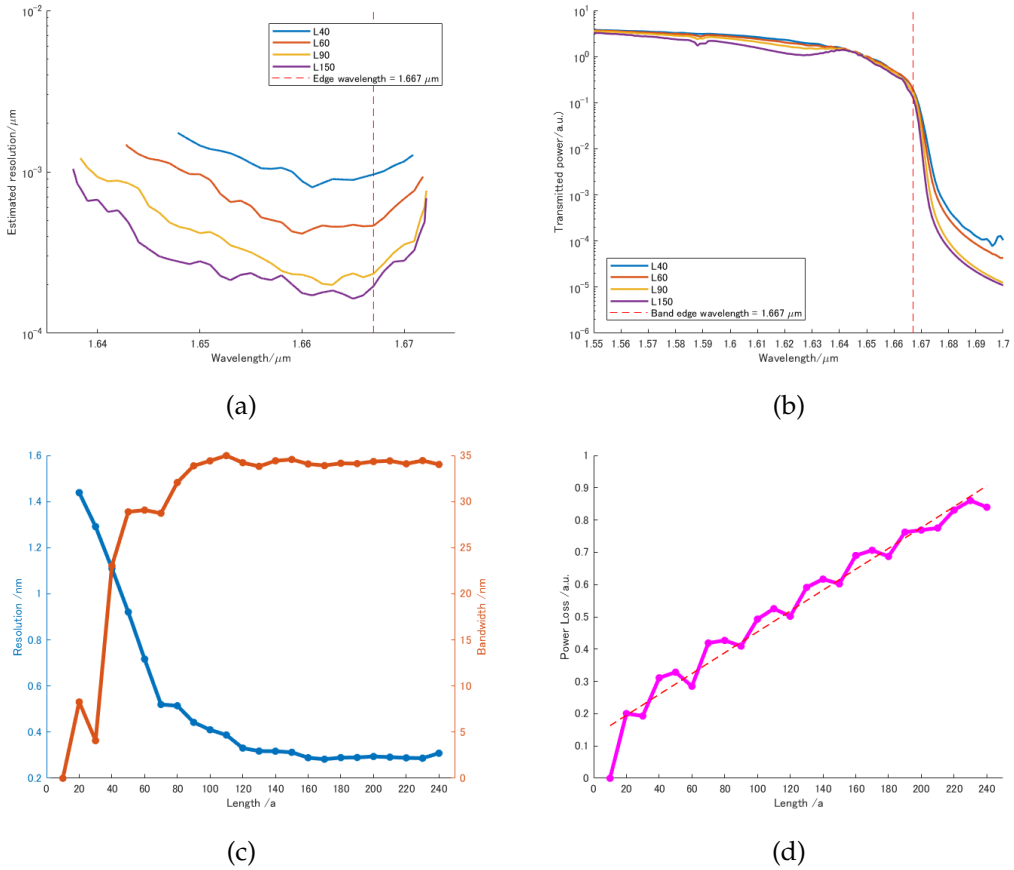

Figure 4.4: (a) Operating range and expected resolutions for section lengths of 40a, 60a, 90a and 150a. (b) Transmittance spectra for section lengths of 40a, 60a, 90a and 150a. (c) Effective bandwidths and effective resolutions for different section lengths. (d) Propagation losses at the wavelength of 1.637 μm for different section lengths. The propagation loss for the 10a section is specified as zero.

Based on the default settings mentioned in Section 3.2, set the number of sections (`PhC.section`) as 1, and vary the total length of the PhC waveguide from 10a to 240a. PhC waveguide structure with random fabrication errors is generated for each run of the simulation.

Figure 4.3 shows the effective bandwidth and effective averaged resolution at different section lengths, which are statistical results over at least 20 runs of simulation for each wavelength. Specifically, 30 runs are carried out for lengths from 10a to 30a, and 20 runs from 40a to 240a.

The tendencies when increasing the section length are concluded in Figure 4.4. The simulation results show that in general a longer PhC waveguide produces a larger effective bandwidth and smaller effective averaged resolution, which means better performance as a spectrometer. This is an expected tendency as the probability that Anderson localization happens is higher in a longer PhC waveguide if the waveguide length is longer than localization length, as explained in Section 2.2.2. Meanwhile, the energy intensity profile data grow with increasing PhC waveguide length, so that more information can be used to reconstruct the input spectrum, resulting in better resolution.

However, both the effective bandwidth and effective averaged resolution almost converge when the length exceeds 120a. Further increase of PhC waveguide length offers minor improvements. When the waveguide length exceeds 120a, the spectrometer meets some limitations that prevent it from notably gain.

First, most of the wavelengths in the Lifshitz tail have reached their localization lengths, as mentioned in Section 2.2. The rest wavelengths' localization lengths are too long and cannot provide evident enough characteristic patterns. For wavelengths with localization lengths smaller than waveguide length, the possibility that Anderson localization happens outside the localization length is very low, so the additional PhC waveguide length barely contributes to the resolution of the spectrometer.

Second, because the step size of sampling wavelengths is 1 nm for all simulations in this work, resolutions smaller than 1 nm are the results of linear interpolations when calculating the Pearson correlation coefficient, which means that the effective averaged resolutions may not have enough precision to show the improvements from the increased PhC waveguide length.

The benefits of increasing section length don't last forever. Meanwhile the propagation loss increases linearly with section length, as shown in Figure 4.4(d), so there is no point in pursuing a section length longer 120a. In the following section we will see that break down the a 120a long PhC waveguide into proper chirped structure can produce better performance.

4.3 Varying the section width reduction rate of the PhC waveguide

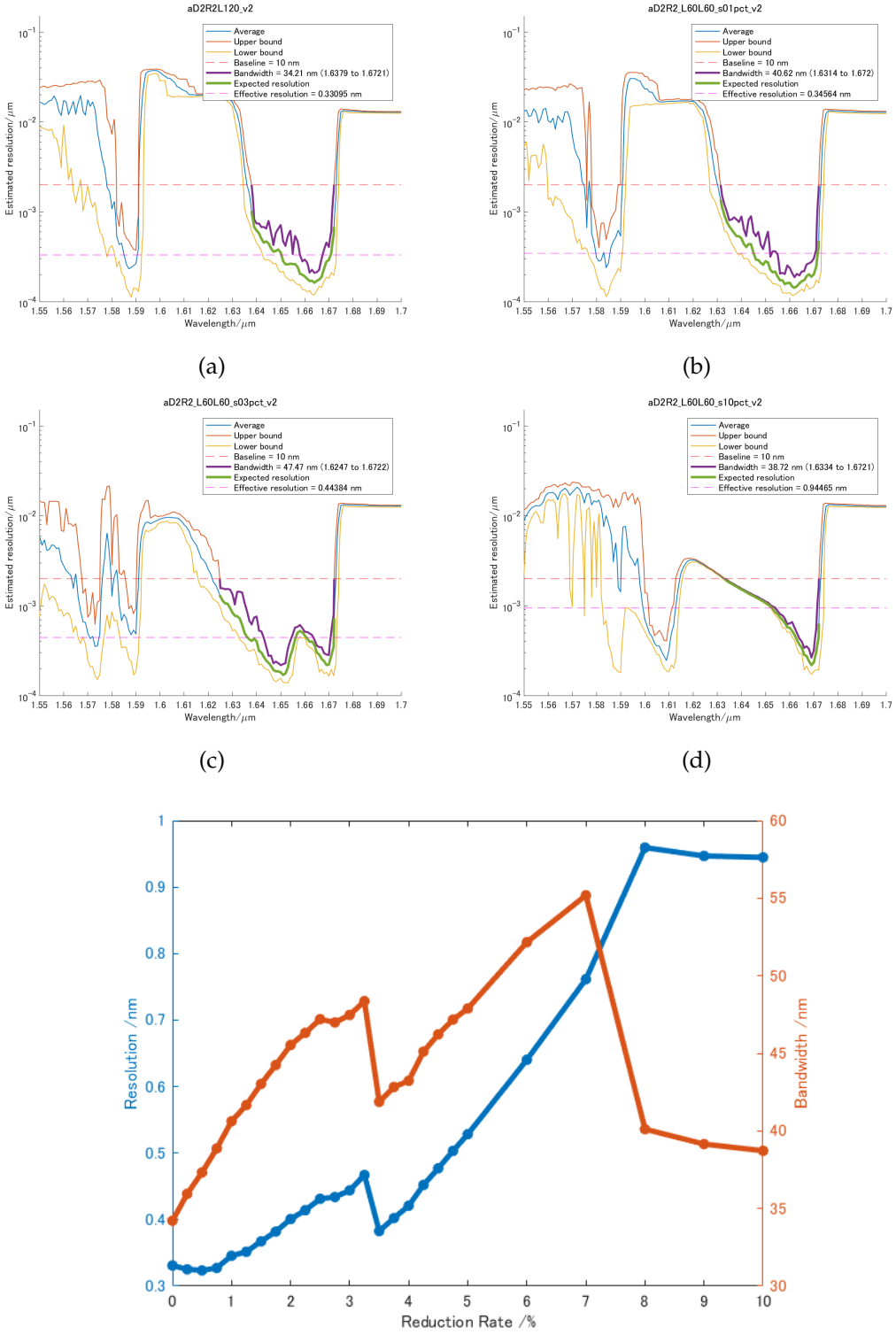

Figure 4.5: (a)-(d) Estimated resolutions of a 60*a*-60*a* structure with reduction rates of 0%, 1%, 3%, and 10%. (e) Effective bandwidths and effective resolutions of a 60*a*-60*a* structure at different reduction rates.

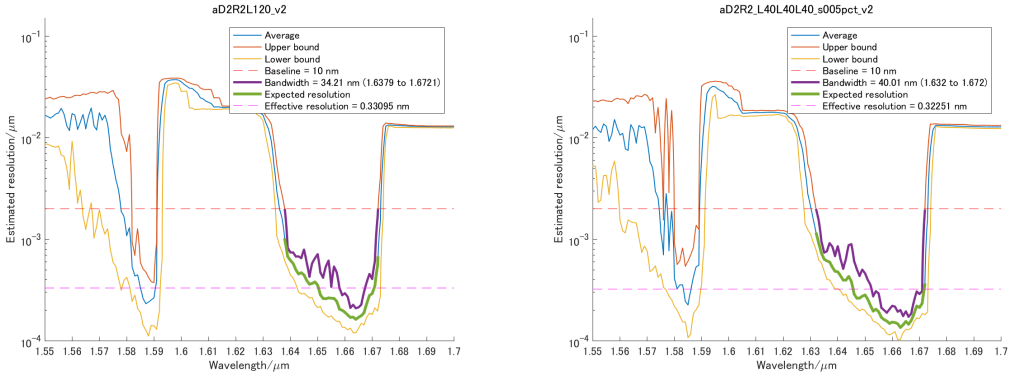

(a)

(b)

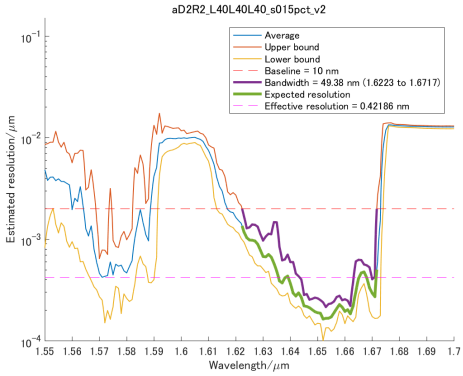

(c)

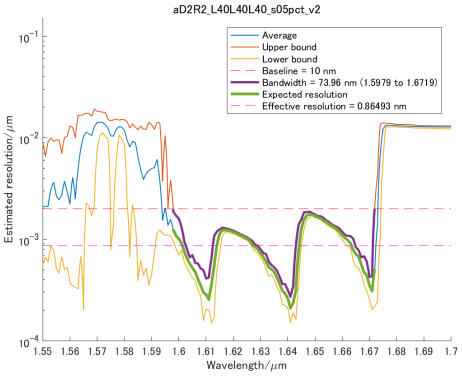

(d)

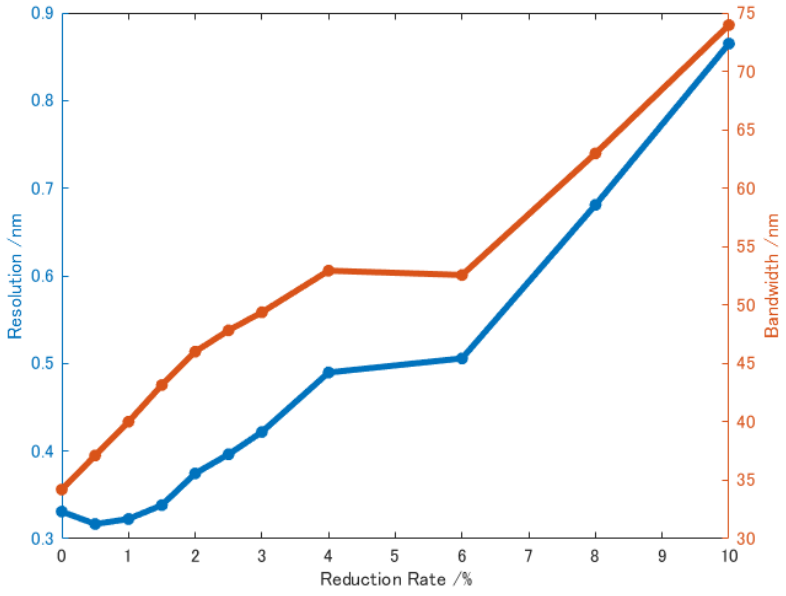

(e)

Figure 4.6: (a)-(d) Estimated resolutions of a 40a-40a-40a structure with total reduction rates of 0%, 1%, 3%, and 10%. (e) Effective bandwidths and effective resolutions of a 40a-40a-40a structure at different total reduction rates.

The motivation of designing a chirped PhC waveguide is to broaden the effective bandwidth. As we show in Section 4.2, the effective bandwidth for a single-section PhC waveguide converges when it reaches a certain length. However, with a chirped structure that connects the operating wavelength range of neighboring sections, as shown in Figure 2.12, the effective bandwidth can be expanded multiple times.

We first investigate a 2-section structure. A $120a$ chirped PhC waveguide is divided by two $60a$ sections. The reduction rate varies from 0% to 10%. The definition of reduction rate is explained in Section 3.2. For each reduction rate, 20 runs are carried out with randomly generated structures every time. The estimated resolutions for reduction rates of 0%, 1%, 3%, and 10% are plotted in Figure 4.5(a)-(d) respectively.

When the reduction rate is small like 1%, the light propagates from a W1 waveguide to W0.99 waveguide. Compared with the 0% reduction $120a$ long PhC waveguide, the bandwidth is efficiently increased, and the resolution is also slightly improved.

Continue increasing the reduction rate to 3%, although the effective bandwidth is further broadened, the resolution gets worse because the originally continuous valley bottom is separate as two narrower valley bottoms, which means the overlapped wavelength range of two sections is reduced.

Further increasing the reduction rate to 10%, the two valley bottoms get more separated and the hilltop exceeds the baseline, thus the effective bandwidth drops and the effective resolution gets worse too.

The tendencies of effective bandwidths and effective averaged resolutions are concluded in Figure 4.5(e). When the reduction rate is smaller than 1%, it has positive effects on both the bandwidth and the resolution, compared with the 0% reduction $120a$ long PhC waveguide. For larger reduction rates, although the bandwidth is increased, the resolution gets worse than 0% condition, which is not a preferred behavior.

Sharp declines for effective bandwidth and effective resolution is observed at reduction rate of 3.5%. This is due to the increased fluctuations of resolutions at shorter wavelength side of the valley, which results in larger "Upper bound" and narrower effective bandwidth. The "Average" itself does not have dramatic change as the "Upper bound", so the maximum value of expected resolutions inside the effective bandwidth gets lower than reduction rate = 3% condition, and the effective averaged resolution gets lower. This kind of decreased effective bandwidth is a common reason for the decrease of effective averaged resolution when processing data, and will appear in next section too.

When reduction rate is larger than 7%, the hilltop between the two separated valleys exceeds the baseline, the function of chirped waveguide that connects effective bandwidths of two section fails.

Conclude the reduction rate for a $60a - 60a$ chirped structure, we found that for reduction rate smaller than 1%, the effective resolution is enhanced than a non-chirped $120a$ long waveguide. Reduction rate between 1% and 3% might be useful if the first priority is effective bandwidth. For the high

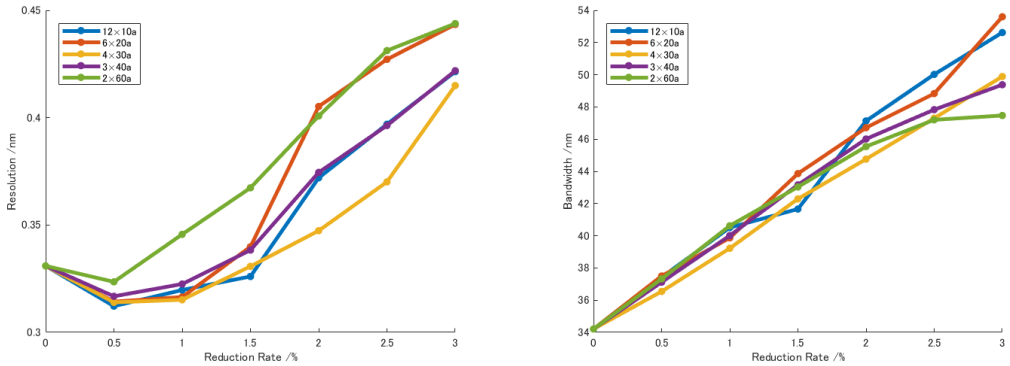

(a) (b)

Figure 4.7: (a) Effective averaged resolutions and (b) effective bandwidths of a 120a-total-length structure at different reduction rates. The combinations of number and length of sections are 12×10a, 6×20a, 4×30a, 3×40a and 2×60a, respectively.

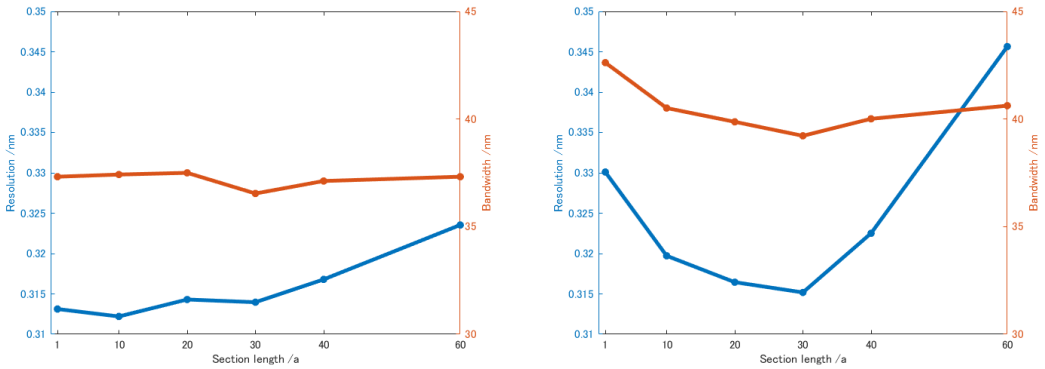

(a) (b)

Figure 4.8: Effective bandwidths and effective resolutions of a 120a-total-length structure at different section lengths. The total reduction rates are (a) 0.5% and (b) 1% respectively.

precision spectrometer target, the optimal reduction rate is between 0% and 1%. Although the best resolution is at 0.5%, the reduction rate of 0.75% is also attractive if consider the gain of bandwidth.

If the total length and expected operating wavelength range of the chirped PhC waveguide are fixed, there are two strategies when designing the structure. We can either use a large number of sections with a small reduction rate, or a small number of sections with a large reduction rate to build the device.

To find out the optimal combination, we simulate a $40a - 40a - 40a$ three-section chirped PhC waveguide structure, with total reduction rate varies from 0% to 10%. Here the total reduction rate is the multiplication of the reduction rate of one section and the number of width reduced sections, e.g., if it is a W1-W0.99-W0.98 chirped waveguide, then the total reduction rate = $1\% \times 2 = 2\%$. The simulation results are shown in Figure 4.6, with 20 runs

for each reduction rate.

In general, the $40a - 40a - 40a$ structure has the similar tendency of effective bandwidth and effective averaged wavelength at different disorder levels as the $60a - 60a$ structure, though there is no sharp decline as found at the 3.5% and 8% reduction rate in the $60a - 60a$ structure. Pay attention to Figure 4.6(d), the hilltops do not exceed the baseline even at the total reduction rate of 10%. The three-section $40a - 40a - 40a$ structure shows better robustness to the separation of effective bandwidth than the two-section $60a - 60a$ structure.

We continue to increase the number of sections and simulate the $4\times30a$, $6\times20a$, and $12\times10a$ structure with total reduction rate varies from 0% to 3%, 10 runs for each reduction rate. The comparison of effective averaged resolutions and effective bandwidths for different number of sections are shown in Figure 4.7. In general the performances for the structures different number of sections are similar at the same total reduction rate. The best effective resolutions are all obtained at the total reduction rate of 0.5%, and the effective bandwidths all grow with increased total reduction rates. Figure 4.7 shows that when the total length of chirped waveguide is fixed, the performance of the spectrometer is mainly defined by the total reduction rate, while the variation of number of sections can provide some additional biases to the effective resolution and effective bandwidth. For example, the $4\times30a$ structure has good resolutions at all total reduction rates, but its bandwidths are poor at the same time.

Rearrange the effective bandwidths and effective resolutions information from Figure 4.7, with the addition of data from 10 runs of $120\times1a$ tapered structure, we conclude the effect of section length (equivalent to the effect of number of sections when total length is fixed) at total reduction rates of 0.5% and 1% respectively in Figure 4.8(a) and (b). We can see that for the total reduction rate of 0.5%, the $12\times10a$ structure has the best effective resolution and a good effective bandwidth, while for the total refuction rate of 1%, the $4\times30a$ structure has the best effective resolution and lowest effective bandwidth at the same time. The optimal combination of section length and number of sections may vary with the total reduction rate, which requires further investigation.

The above-mentioned research results are focused on a total length of $120a$, and suggests that a total reduction rate of 0.5% is optimal when the high resolution is the first priority. Simulations of other total lengths indicate that the optimal total reduction rate of waveguide width may change non-linearly with the total length, which requires further acquisition and processing of data.

4.4 Varying the disorder level of the PhC waveguide

Finally, we roughly investigate how the disorder level will affect the performance of the chirped PhC waveguide spectrometer. $120a$ long single

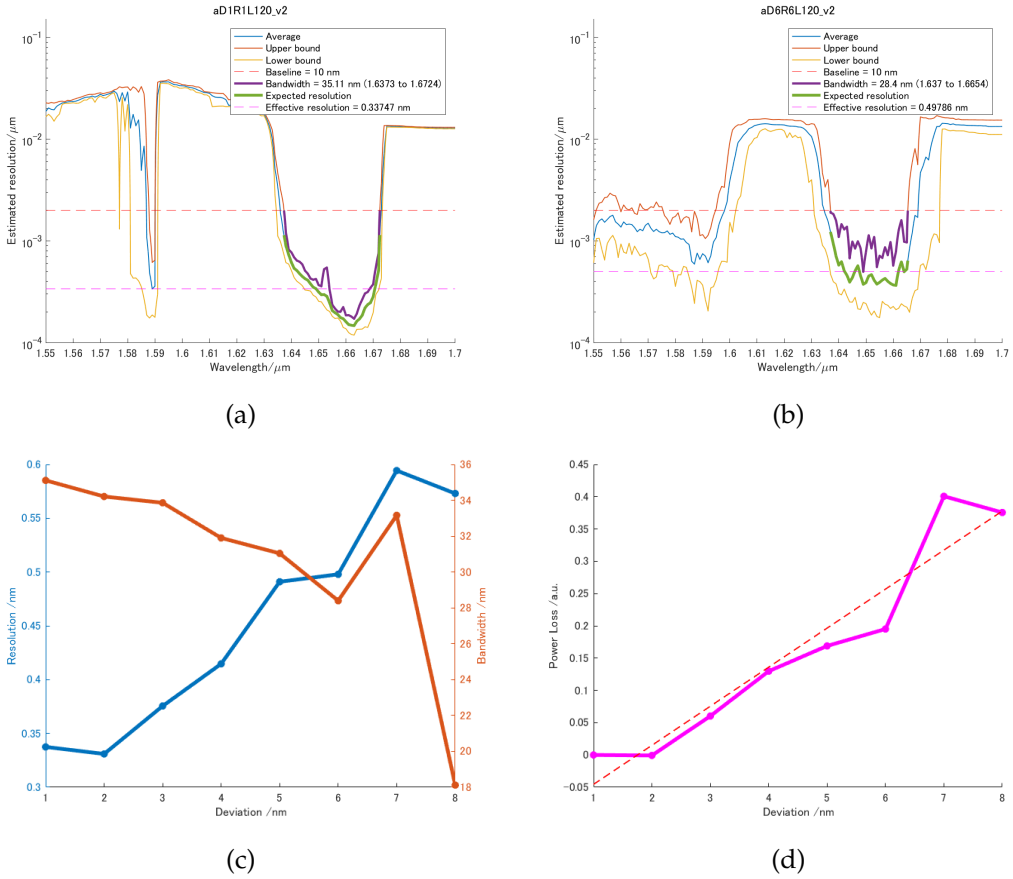

Figure 4.9: Estimated resolutions for a 120a single section structure with disorder (a) $\sigma = 1$ nm, (b) $\sigma = 6$ nm. (c) Effective bandwidths and effective resolutions of a 120a long single section structure for different disorder levels. (d) Propagation losses of a 120a long single section structure at the wavelength of 1.637 μm for different disorder levels. The propagation loss for the 10a section is specified as zero.

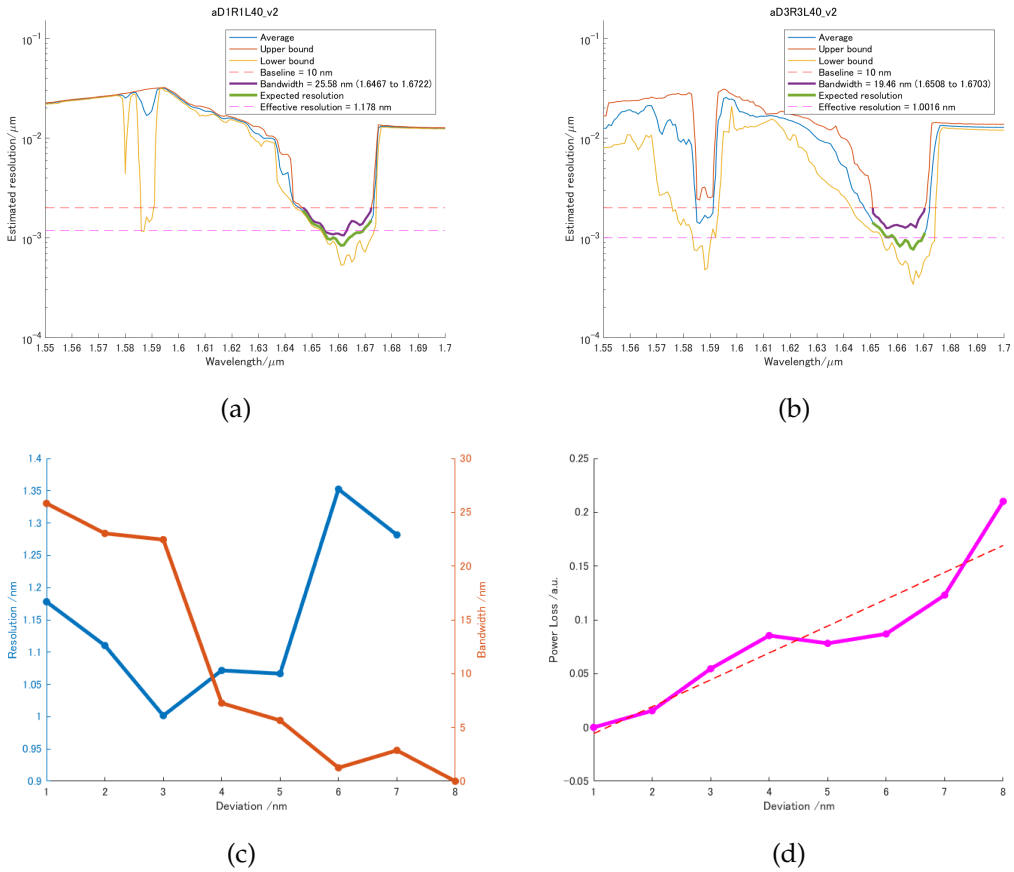

Figure 4.10: Estimated resolutions for a 40a single section structure with disorder (a) $\sigma = 1$ nm, (b) $\sigma = 3$ nm. (c) Effective bandwidths and effective resolutions of a 40a long single section structure for different disorder levels. (d) Propagation losses of a 40a long single section structure at the wavelength of 1.637 μm for different disorder levels. The propagation loss for the 10a section is specified as zero.

section waveguides with different amount of disorder are simulated, 10 runs for each disorder level respectively. The disorder is set as $\sigma = \sigma_r = \sigma_d$, ranging from 1 nm ($\sim$0.002$a$) to 6 nm ($\sim$0.014$a$). The calculated effective bandwidths and effective averaged resolutions are plotted in Figure 4.9(c) and the variation of propagation loss is plotted in Figure 4.9(d). Although the results do not converge well due to the limited number of realizations, we can still find out that in general as the amount of disorder increases, the effective bandwidth becomes smaller, the effective averaged resolution becomes larger, and the propagation loss also increases. It seems like for a 120a long waveguide, all aspects of its performance as a spectrometer get worse when the amount of disorder increases. Although the effective resolution of $\sigma = 2$ nm is slightly better than $\sigma = 1$ nm, this could be the effect of reduced effective bandwidth or statistical error due to limited number of samples.

The higher propagation loss is expected as the increase or disorder lead to more back-scattering and more in-plane loss through photonic crystal rows because of the broken Bragg reflection. The deteriorated effective bandwidth and effective resolution are though confusing because as mentioned in section 2.2.1 the width of the Lifshitz tail is supposed to extend when the amount of disorder is increased, which sound like a promise for the growth of effective bandwidth.

The contradiction here comes from our definition of effective bandwidth, as we focus on the upper bound of statistical resolution and define the spectral range where the upper bound is below the baseline as the effective bandwidth. The reason to use the upper bound is to ensure that every (or at least most of) realization of PhC waveguide at that disorder level is guaranteed to provide resolutions better than the baseline in the effective bandwidth. Compare the estimated resolutions plots of $\sigma = 1$ nm (Figure 4.9(a)) with $\sigma = 6$ nm (Figure 4.9(b)), it is obvious that the upper bound and lower bound of resolutions get more separated in $\sigma = 6$ nm situation, which means the performance of $\sigma = 6$ nm devices becomes much more unstable. Pay attention to the crossover of lower bound and baseline in Figure 4.9(a) and Figure 4.9(b), it is the extended lower bound that refers to the actual broadened Lifshitz tail. Furthermore, as can be seen from Figure 2.7(c), when the Lifshitz tail width increases with the amount of disorder, the localized modes becomes more and more diffused in spectrum for an individual test subject, which means the characteristic patterns become sparse in spectral domain and lowers the resolution of the spectrometer.

However, consider the fact that the localization length decreases with increasing amount of disorder, high disorder level might have some advantages at shorter section lengths. Figure 4.10(c) plots the effective bandwidths and effective averaged resolutions of a 40a long PhC waveguide with different amount of disorder. The best resolution is at $\sigma = 3$ nm, which matches our guess. Compare the details of estimated resolutions of $\sigma = 1$ nm and $\sigma = 3$ nm in Figure 4.10(a) and (b), the better effective resolution of $\sigma = 3$ nm is mainly due to the reduced effective bandwidth, caused by larger fluctuations of resolution. Nonetheless, the lower bound of $\sigma = 3$ nm

has lower minimum value than $\sigma = 1$ nm, which could be the consequence of shorter localization length.

In conclusion, as the disorder level increases, the increased fluctuations in band structure cause more unstable resolutions which shorten the effective bandwidth, and the spread of Anderson localized modes reduce the averaged resolution. Although stronger localization are found in PhC waveguides with high disorder level, the small amount of disorder is preferable for the stable performance when disordered PhC waveguides are used as parts of reconstructive spectrometers. However, the shorter localization length of high disorder level may contain the potential to help build chirped PhC waveguide with shorter section length, thus miniaturize the footprint of the spectrometer.

Chapter 5

Summary and Outlook

5.1 Summary

In summary, I introduced an on-chip spectrometer prototype designed by Tanabe Lab, which uses simple and low-cost photonic crystal structures and utilizes random fabrication errors to enhance resolution. My investigation on performance analysis at varying geometry parameters shows that under the disorder level of $\sigma = 2$ nm, single section length should not exceed the localization length around $120a$, and for a chirped waveguide with total length of $120a$, the total reduction rate is optimal around 0.5% per section to ensure high resolution. For a more straightforward presentation, with the lattice constant $a = 420$ nm and a W1 PhC waveguide (waveguide width 727.461 nm) as the first section, if we set the section length as $60a$ (25.2 µm), reduction rate of 0.5% per section (3.637 nm per section), 20 sections in total, we can expect a spectrometer with a resolution around 0.3 nm, a bandwidth around 93.3 nm, and a total length of chirped waveguide of 0.504 mm, under the assumption of a linearly increase of effective bandwidth with the total length.

The investigation of disorder level indicates that photonic crystal waveguides with large amount of disorder are not suitable for building spectrometer due to their unstable performance, while the disorder level of $\sigma = 2$ nm is reliable and matches state-of-the-art fabrication techniques. There is a possibility that the device length can be shorten with a slightly higher disorder level like $\sigma = 3$ nm, which requires further research.

5.2 Future works and outlook

The biggest obstacle in this work is the long simulation time with FDTD method. On the six-core desktop computer "hpc03" from Tanabe Lab, it takes about 16 minutes for a single run of a $40a$-long structure, about 180 minutes for a single run of a $120a$-long structure, about 520 minutes for a single run of a $240a$-long structure, with a 6 threads multiprocessing setting. While in practical chips, the chirped PhC waveguide could have a total length $20\times80a = 1600a$, the exponentially growth of simulation time hinders us from researching longer structures by numerical method. Besides, many compromises are made in the simulation setting to save time and gain more data. The coupling section connecting the rectangular waveguide and the

PhC waveguide is omitted to reduce the simulation domain, which affects the coupling efficiency of wavelengths close to band edge, especially those in evanescent regime, so their Anderson localization are most likely suppressed in simulations. Also, the five rows of photonic crystal holes on both sides of the line defect are actually not enough to confine light in transverse directions, which increase the propagation losses.

The best solution is to find the simulation method with higher efficiency. The Bloch mode expansion method mentioned in Savona's work [31] seems attractive as it is claimed that a 1024a-long W1 PhC waveguide can be simulated within a few hours on a desktop computer. However, this method can only calculate the eigenmodes so I am not sure it can simulate the time variant propagating of light in waveguide and the steady-states field that we are interested in. Compared with the overlong FDTD simulation time, fabricating new chips and testing the performances experimentally is a more reliable solution.

As for the commercial application of the chirped PhC waveguide spectrometer, there is a long distance. One essential topic is the integration of sensor unit. We can continue the current method by integrating the infrared camera and lens into a package with chirped PhC waveguide chip, or use probes on top the chip to collect scattered light like the SWIFTS shown in Ref. [21].

References

[1] Z. Y. Yang, T. Albrow-Owen, W. W. Cai, and T. Hasan, "Miniaturization of optical spectrometers," *Science*, vol. 371, no. 6528, eabe0722, Jan. 2021, ISSN: 1095-9203. DOI: 10.1126/science.abe0722.

[2] T. Yokino, K. Kato, A. Ui, *et al.*, "Grating-based ultra-compact SWNIR spectral sensor head developed through MOEMS technology," *Moems and Miniaturized Systems Xviii*, vol. 10931, p. 1 093 108, 2019. DOI: 10.1117/12.2510472.

[3] D. S. GOLDMAN, P. L. WHITE, and N. C. ANHEIER, "Miniaturized spectrometer employing planar wave-guides and grating couplers for chemical-analysis," *Applied Optics*, vol. 29, no. 31, pp. 4583–4589, Nov. 1990. DOI: 10.1364/AO.29.004583.

[4] B. S. Gao, Z. M. Shi, and R. W. Boyd, "Design of flat-band superprism structures for on-chip spectroscopy," *Optics Express*, vol. 23, no. 5, pp. 6491–6496, Mar. 2015, ISSN: 1094-4087. DOI: 10.1364/OE.23.006491.

[5] G. Calafiore, A. Koshelev, S. Dhuey, *et al.*, "Holographic planar lightwave circuit for on-chip spectroscopy," *Light-Science & Applications*, vol. 3, no. 9, e203, Sep. 2014, ISSN: 2047-7538. DOI: 10.1038/lsa.2014.84.

[6] M. Ebermann, N. Neumann, K. Hiller, M. Seifert, M. Meinig, and S. Kurth, "Tunable MEMS Fabry-Perot filters for infrared microspectrometers: A review," in *MOEMS and Miniaturized Systems XV*, W. Piyawattanametha and Y.-H. Park, Eds., vol. 9760, SPIE, Mar. 2016, 97600H. DOI: 10.1117/12.2209288.

[7] N. Neumann, M. Ebermann, and S. Kurth, "Tunable infrared detector with integrated micromachined Fabry-Perot filter," *Journal of Micro-Nanolithography Mems and Moems*, vol. 7, no. 2, p. 021 004, Apr. 2008, ISSN: 1932-5150. DOI: 10.1117/1.2909206.

[8] J. H. Correia, G. de Graaf, S. H. Kong, M. Bartek, and R. F. Wolffenbuttel, "Single-chip CMOS optical microspectrometer," *Sensors and Actuators A: Physical*, vol. 82, no. 1-3, pp. 191–197, May 2000, ISSN: 0924-4247. DOI: 10.1016/S0924-4247(99)00369-6.

[9] Q. Hang, B. Ung, I. Syed, N. Guo, and M. Skorobogatiy, "Photonic bandgap fiber bundle spectrometer," *Applied Optics*, vol. 49, no. 25, pp. 4791–4800, Sep. 2010, ISSN: 1539-4522. DOI: 10.1364/AO.49.004791.

[10] J. H. JERMAN, D. J. CLIFT, and S. R. MALLINSON, "A miniature Fabry-Perot-interferometer with a corrugated silicon diaphragm support," *Sensors and Actuators A: Physical*, vol. 29, no. 2, pp. 151–158, Nov. 1991, ISSN: 0924-4247. DOI: 10.1016/0924-4247(91)87117-L.

[11] J. Antila, A. Miranto, J. Mäkynen, *et al.*, "MEMS and piezo actuator based Fabry-Perot interferometer technologies and applications at VTT," in *Next-Generation Spectroscopic Technologies III*, M. A. Druy, C. D. Brown, and R. A. Crocombe, Eds., vol. 7680, SPIE, Apr. 2010, 76800U. DOI: 10.1117/12.850164.

[12] S. W. Wang, C. S. Xia, X. S. Chen, *et al.*, "Concept of a high-resolution miniature spectrometer using an integrated filter array," *Optics Letters*, vol. 32, no. 6, pp. 632–634, Mar. 2007, ISSN: 1539-4794. DOI: 10.1364/OL.32.000632.

[13] N. K. Pervez, W. Cheng, Z. Jia, M. P. Cox, H. M. Edrees, and I. Kymissis, "Photonic crystal spectrometer," *Optics Express*, vol. 18, no. 8, pp. 8277–8285, Apr. 2010, ISSN: 1094-4087. DOI: 10.1364/OE.18.008277.

[14] A. Tittl, A. Leitis, M. K. Liu, *et al.*, "Imaging-based molecular barcoding with pixelated dielectric metasurfaces," *Science*, vol. 360, no. 6393, pp. 1105–+, Jun. 2018, ISSN: 1095-9203. DOI: 10.1126/science.aas9768.

[15] A. Nitkowski, L. Chen, and M. Lipson, "Cavity-enhanced on-chip absorption spectroscopy using microring resonators," *Optics Express*, vol. 16, no. 16, pp. 11 930–11 936, Aug. 2008, ISSN: 1094-4087. DOI: 10.1364/OE.16.011930.

[16] A. Emadi, H. W. Wu, G. de Graaf, and R. Wolffenbuttel, "Design and implementation of a sub-nm resolution microspectrometer based on a linear-variable optical filter," *Optics Express*, vol. 20, no. 1, pp. 489–507, Jan. 2012, ISSN: 1094-4087. DOI: 10.1364/OE.20.000489.

[17] R. G. DeCorby, N. Ponnampalam, E. Epp, T. Allen, and J. N. McMullin, "Chip-scale spectrometry based on tapered hollow Bragg waveguides," *Optics Express*, vol. 17, no. 19, pp. 16 632–16 645, Sep. 2009, ISSN: 1094-4087. DOI: 10.1364/OE.17.016632.

[18] O. Manzardo, H. P. Herzig, C. R. Marxer, and N. F. de Rooij, "Miniaturized time-scanning Fourier transform spectrometer based on silicon technology," *Optics Letters*, vol. 24, no. 23, pp. 1705–1707, Dec. 1999, ISSN: 1539-4794. DOI: 10.1364/OL.24.001705.

[19] K. Wang, J. Y. Li, D. F. Lu, and Z. M. Qi, "Algorithmic enhancement of spectral resolution of a lithium niobate ($LiNbO_3$) waveguide-based miniature Fourier transform spectrometer," *Applied Spectroscopy*, vol. 70, no. 10, pp. 1685–1691, Jul. 2016, ISSN: 1943-3530. DOI: 10.1177/0003702816644454.

[20] M. C. M. M. Souza, A. Grieco, N. C. Frateschi, and Y. Fainman, "Fourier transform spectrometer on silicon with thermo-optic non-linearity and dispersion correction," *Nature Communications*, vol. 9, no. 1, p. 665, Feb. 2018, ISSN: 2041-1723. DOI: 10.1038/s41467-018-03004-6.

[21] D. Pohl, M. R. Escalé, M. Madi, *et al.*, "An integrated broadband spectrometer on thin-film lithium niobate," *Nature Photonics*, vol. 14, no. 1, pp. 24–+, Jan. 2020. DOI: 10.1038/s41566-019-0529-9.

[22] J. Y. Li, D. F. Lu, and Z. M. Qi, "Miniature Fourier transform spectrometer based on wavelength dependence of half-wave voltage of a $LiNbO_3$ waveguide interferometer," *Optics Letters*, vol. 39, no. 13, pp. 3923–3926, Jun. 2014, ISSN: 1539-4794. DOI: 10.1364/OL.39.003923.

[23] S. N. Zheng, J. Zou, H. Cai, *et al.*, "Microring resonator-assisted Fourier transform spectrometer with enhanced resolution and large bandwidth in single chip solution," *Nature Communications*, vol. 10, no. 1, p. 2349, May 2019, ISSN: 2041-1723. DOI: 10.1038/s41467-019-10282-1.

[24] B. Redding, S. F. Liew, R. Sarma, and H. Cao, "Compact spectrometer based on a disordered photonic chip," *Nature Photonics*, vol. 7, no. 9, pp. 746–751, Jul. 2013, ISSN: 1749-4893. DOI: 10.1038/NPHOTON.2013.190.

[25] B. Redding, S. F. Liew, Y. Bromberg, R. Sarma, and H. Cao, "Evanescently coupled multimode spiral spectrometer," *Optica*, vol. 3, no. 9, pp. 956–962, Sep. 2016, ISSN: 2334-2536. DOI: 10.1364/OPTICA.3.000956.

[26] Z. Wang and Z. F. Yu, "Spectral analysis based on compressive sensing in nanophotonic structures," *Optics Express*, vol. 22, no. 21, pp. 25 608–25 614, Oct. 2014, ISSN: 1094-4087. DOI: 10.1364/OE.22.025608.

[27] S. Zhang, Y. H. Dong, H. Y. Fu, S. L. Huang, and L. Zhang, "A spectral reconstruction algorithm of miniature spectrometer based on sparse optimization and dictionary learning," *Sensors*, vol. 18, no. 2, p. 644, Feb. 2018, ISSN: 1424-8220. DOI: 10.3390/s18020644.

[28] T. Kodama, J. Hofs, S. J. Jin, and T. Tanabe, "High-resolution spectrometer with random photonic crystals," *2020 Conference on Lasers and Electro-Optics (cleo)*, IEEE, 2020. [Online]. Available: https://ieeexplore.ieee.org/abstract/document/9192107.

[29] J. D. Joannopoulos, S. G. Johnson, J. N. Winn, and R. D. Meade, *Photonic Crystals: Molding the Flow of Light - Second Edition*. Princeton University Press, Dec. 2008, pp. 1–286, ISBN: 9781400828241. DOI: 10.1515/9781400828241.

[30] T. F. Krauss, "Slow light in photonic crystal waveguides," *Journal of Physics D: Applied Physics*, vol. 40, no. 9, pp. 2666–2670, May 2007, ISSN: 1361-6463. DOI: 10.1088/0022-3727/40/9/S07.

[31] V. Savona, "Electromagnetic modes of a disordered photonic crystal," *Physical Review B*, vol. 83, no. 8, p. 085 301, Feb. 2011, ISSN: 1550-235X. DOI: 10.1103/PhysRevB.83.085301.

[32] P. D. García and P. Lodahl, "Physics of quantum light emitters in disordered photonic nanostructures," *Annalen Der Physik*, vol. 529, no. 8, p. 1 600 351, Aug. 2017, ISSN: 1521-3889. DOI: 10.1002/andp.201600351.

[33] J. Topolancik, F. Vollmer, and B. Ilic, "Random high-Q cavities in disordered photonic crystal waveguides," *Applied Physics Letters*, vol. 91, no. 20, p. 201 102, Nov. 2007, ISSN: 1077-3118. DOI: 10.1063/1.2809614.

[34] L. Sapienza, H. Thyrrestrup, S. Stobbe, P. D. Garcia, S. Smolka, and P. Lodahl, "Cavity quantum electrodynamics with Anderson-localized modes," *Science*, vol. 327, no. 5971, pp. 1352–1355, Mar. 2010, ISSN: 1095-9203. DOI: 10.1126/science.1185080.

[35] P. D. García, A. Javadi, H. Thyrrestrup, and P. Lodahl, "Quantifying the intrinsic amount of fabrication disorder in photonic-crystal waveguides from optical far-field intensity measurements," *Applied Physics Letters*, vol. 102, no. 3, p. 031 101, Jan. 2013, ISSN: 1077-3118. DOI: 10.1063/1.4788709.

[36] I. Lifshitz, "The energy spectrum of disordered systems," *Advances in Physics*, vol. 13, no. 52, pp. 483–536, Oct. 1964, ISSN: 1460-6976. DOI: 10.1080/00018736400101061.

[37] P. D. García, G. Kirsanske, A. Javadi, S. Stobbe, and P. Lodahl, "Two mechanisms of disorder-induced localization in photonic-crystal waveguides," *Physical Review B*, vol. 96, no. 14, p. 144 201, Oct. 2017, ISSN: 2469-9969. DOI: 10.1103/PhysRevB.96.144201.

[38] P. D. García, S. Smolka, S. Stobbe, and P. Lodahl, "Density of states controls Anderson localization in disordered photonic crystal waveguides," *Physical Review B*, vol. 82, no. 16, p. 165 103, Oct. 2010, ISSN: 1550-235X. DOI: 10.1103/PhysRevB.82.165103.

[39] J. Hofs, T. Kodama, S. J. Jin, and T. Tanabe, "Breaking the fabrication determined resolution limit of photonic crystal wavemeter by machine learning," *2020 Conference on Lasers and Electro-Optics (cleo)*, CLEO_SI, IEEE, 2020. DOI: 10.1364/CLEO_SI.2020.SF1J.4.

[40] A. Beck and M. Teboulle, "A fast iterative shrinkage-thresholding algorithm for linear inverse problems," *Siam Journal on Imaging Sciences*, vol. 2, no. 1, pp. 183–202, Jan. 2009, ISSN: 1936-4954. DOI: 10.1137/080716542.

[41] A. F. Oskooi, D. Roundy, M. Ibanescu, P. Bermel, J. D. Joannopoulos, and S. G. Johnson, "MEEP: A flexible free-software package for electromagnetic simulations by the FDTD method," *Computer Physics Communications*, vol. 181, no. 3, pp. 687–702, Mar. 2010, ISSN: 0010-4655. DOI: 10.1016/j.cpc.2009.11.008.

[42] M. Qiu, "Effective index method for heterostructure-slab-waveguide-based two-dimensional photonic crystals," *Applied Physics Letters*, vol. 81, no. 7, pp. 1163–1165, Aug. 2002, ISSN: 1077-3118. DOI: 10.1063/1.1500774.

[43] J. Benesty, J. Chen, Y. Huang, and I. Cohen, *Noise Reduction in Speech Processing*. Springer Berlin Heidelberg, 2009, vol. 2, pp. 1–229, ISBN: 9783642002960. DOI: 10.1007/978-3-642-00296-0.